Herpes simplex virus 1 protein pUL21 stimulates cellular ceramide transport by activating CERT

Tomasz H. Benedyk[1,a], Viv Connor[1], Eve R. Caroe[2,b], Maria Shamin[2], Dmitri I. Svergun[3], Janet E. Deane[2], Cy M. Jeffries[3], Colin M. Crump[1], Stephen C. Graham[1]*

[1]Department of Pathology, University of Cambridge, Tennis Court Road, Cambridge, UK

[2]Cambridge Institute for Medical Research, University of Cambridge, Cambridge Biomedical Campus, Cambridge, UK

[3]European Molecular Biology Laboratory (EMBL) Hamburg Site, c/o DESY, Notkestrasse 85, Hamburg, Germany

[a]Current address: EG427 Pinpoint Gene Therapy, 29 Rue du Faubourg Saint-Jacques, Paris, France

[b]Current address: The Francis Crick Institute, 1 Midland Road, London, UK

***Corresponding author:** scg34@cam.ac.uk

ORCIDs: THB 0000-0001-6420-3665; ERC 0000-0003-3529-024X; MS 0000-0002-7291-2530; DIS 0000-0003-0830-5696; JED 0000-0002-4863-0330; CMJ 0000-0002-8718-7343; CMC 0000-0001-9918-9998; SCG 0000-0003-4547-4034

Short title: HSV-1 pUL21 modulates cellular ceramide transport

Contributions: Conceptualization: SCG; Data Curation: THB, CMJ, SCG; Funding Acquisition: JED, CMC, SCG; Investigation: THB, VC, ERC, MS, CMJ, CMC, SCG; Project Administration: SCG; Resources: DIS, JED; Supervision: CMC, SCG; Visualization: THB, SCG; Writing – Original Draft Preparation: THB, SCG; Writing – Review & Editing: THB, JED, CMJ, CMC, SCG.

Abstract

Herpes simplex virus (HSV)-1 dramatically alters the architecture and protein composition of cellular membranes during infection, but its effects upon membrane lipid composition remain unclear. HSV-1 pUL21 is a virus-encoded protein phosphatase adaptor that promotes dephosphorylation of multiple cellular and virus proteins, including the cellular ceramide transport protein CERT. CERT mediates non-vesicular transport of ceramide from the ER to the *trans*-Golgi network, whereupon ceramide is converted to sphingomyelin and other sphingolipids that play important roles in cell proliferation, cell signalling and membrane trafficking. Using click chemistry to profile the kinetics of sphingolipid metabolism in cultured cells, we show that pUL21-mediated dephosphorylation activates CERT and increases the rate of ceramide to sphingomyelin conversion. Purified pUL21 and full-length CERT interact with sub-micromolar affinity and we map the domains responsible for the interaction. Solving the solution structure of the pUL21 C-terminal domain in complex with the CERT PH and START domains using small-angle X-ray scattering allows us to identify a single amino acid mutation on the surface of pUL21 that disrupts CERT binding *in vitro* and in cultured cells. Sphingolipid profiling demonstrates that ceramide to sphingomyelin conversion is severely diminished in the context of HSV-1 infection, a defect that is compounded when infecting with a virus encoding the mutated form of pUL21 that lacks the ability to activate CERT. The accumulation of ceramide in the pUL21 mutant virus infection is correlated with accelerated virus replication, illuminating how HSV-1 manipulates lipid metabolism via altering protein phosphorylation to fine-tune its replication.

Introduction

Herpes simplex virus (HSV)-1 is a human pathogen that is estimated to infect the majority of the human population, causing a life-long latent infection [1]. Like all alphaherpesviruses, latent HSV-1 resides in sensory or sympathetic neurons, migrating to the periphery in periodic reactivation events throughout the lifetime of the host. In order to sustain acute (lytic) infection, HSV-1 drastically modifies infected cells [2–5]. In particular, the virus extensively remodels the composition and architecture of cellular membranes to facilitate virus assembly and spread. Nascent capsids leave the nucleus via sequential envelopment and de-envelopment at the inner and outer nuclear membranes [6]. These cytosolic capsids acquire a proteinaceous layer termed 'tegument' and bud into the lumen of post-Golgi membranes that are studded with viral glycoproteins (so called 'secondary envelopment') [7]. The resultant virus-containing vesicles are transported to cell contact sites where they release the mature virus particles to disseminate the infection [8].

HSV-1 pUL21 is a tegument protein that is conserved in all alphaherpesviruses [9]. This multifunctional protein and its homologues are known to interact with multiple cellular and viral partners, including pUL16 [10,11], pUL11 [12], gE [12], tubulin [13] and Roadblock-1 [14], and it has been implicated in a number of important processes including capsid nuclear egress [15], viral cell-to-cell spread [12,16], and retrograde transport along axons to the neuronal cell bodies where latency is established [14,17]. Mutant HSV-1 lacking pUL21 expression exhibits a 10- to 100-fold replication defect and severely impaired cell-to-cell spread, both of which can be at least partially ascribed to the phosphomodulatory role of pUL21 as a protein phosphatase 1 (PP1) adaptor [18]. PP1 is a highly active and abundant cellular phosphatase [19] and pUL21 recruits PP1 to promote dephosphorylation of multiple substrates, including the viral protein pUL31 that is implicated in viral nuclear egress [18,20] and the cellular protein CERT that regulates sphingomyelin metabolism [18].

The cytoplasmic ceramide transport protein CERT (a.k.a. Goodpasture's antigen binding protein, GPBP, encoded by the gene *COL4A3BP*) mediates the non-vesicular trafficking of ceramide from the endoplasmic reticulum (ER) to the *trans*-Golgi network (TGN) and, in doing so, defines the rate of sphingomyelin synthesis [21–23]. CERT contains two well-folded globular domains: an N-terminal pleckstrin homology (PH) domain that mediates its interaction with TGN membranes by binding phosphatidylinositol 4-phosphate, and a C-terminal steroidogenic acute regulatory related lipid transfer (START) domain that directly binds ceramide to mediate its transfer [23]. Crystal structures of both domains have been solved [24,25]. The 'middle region' (MR) that connects the PH and START domains of CERT does not adopt a globular fold, instead containing a coiled-coil region that is likely to mediate CERT self-association [26], a 'two phenylalanines in an acidic tract' (FFAT) motif that recruits CERT to the ER membranes via binding proteins VAPA and VAPB [27], and a serine-rich motif (SRM), hyperphosphorylation of which represses CERT activity [28]. In cultured HeLa cells the vast majority of CERT is in an inactive, hyperphosphorylated state ($CERT^{P}$), available to be mobilised via dephosphorylation to increase the rate of ER-to-TGN ceramide transport in response to stimuli such as sphingomyelin depletion [28].

77 Ceramide (Cer) and sphingolipids like sphingomyelin (SM) are essential for mammalian cell growth and
78 they play important roles in cell signalling, apoptosis and membrane trafficking [29]. Furthermore,
79 sphingolipids and cholesterol participate in the formation of membrane microdomains (including 'lipid
80 rafts') that compartmentalise the lipid and protein composition of cellular membranes [30]. This
81 compartmentalisation is especially important in highly polarised cells such as neurons [31]. Although
82 sphingolipids are crucial to host-cell biology, relatively little is known about the interaction between
83 pathogens and cellular sphingolipid metabolism. The bacteria *Chlamydia trachomatis* is known to
84 directly recruit CERT to bacteria-containing intracellular inclusions, thereby increasing the abundance
85 of SM in the inclusion membrane [32], and CERT activity is necessary for the biosynthesis of double-
86 membrane vesicles that serve as the sites of hepatitis C virus and polio virus replication [33]. However,
87 to the best of our knowledge, the binding of CERT to HSV-1 pUL21 [18] is the only known example of
88 a direct interaction between CERT and a virus protein.

89 Previous studies have shown that HSV-1 infection increases Cer synthesis [34] and that depletion of
90 sphingomyelinase causes a >30-fold decrease in HSV-1 replication [35]. Sphingomyelinase treatment
91 of cultured epithelial cells has only a very modest effect upon HSV-1 entry [36], suggesting that SM is
92 not absolutely required for virus infection. In contrast, recent studies in macrophages demonstrated that
93 acid ceramidase activity is potently antiviral, helping sequester incoming virus particles by promoting
94 their neutralising association with sphingosine-rich intraluminal vesicles within endocytic multi-vesicular
95 bodies [37]. Furthermore, siRNA depletion of CERT has been shown to promote secretion of usually
96 cell-associated HSV-1 virions [38]. It is therefore increasingly clear that cellular sphingolipid metabolism
97 is important for HSV-1 biology, and that further studies are required to obtain a full picture of how specific
98 sphingolipids support and/or prevent HSV-1 infection.

99 We sought to define the functional consequences of the pUL21:CERT interaction for HSV-1 infection.
100 Using click-chemistry we demonstrated that pUL21-mediated CERT dephosphorylation increases the
101 rate of Cer to SM conversion in cultured cells. We characterised the solution structure of the pUL21 C-
102 terminal domain in complex with the PH and START domains of CERT, identifying a specific pUL21
103 amino acid required for the interaction. Functional characterisation of mutant HSV-1 encoding this
104 mutated form of pUL21 confirmed that pUL21-mediated CERT dephosphorylation alters the rate of SM
105 synthesis in infected cells. Furthermore, we observed a dramatic increase in the rate of Cer synthesis
106 in infected cells, which was only partly counteracted by pUL21-stimulated CERT activity, and that this
107 increase in Cer abundance correlated with accelerated virus replication.

Results

Human cells typically maintain lipidome homeostasis via robust feedback and control mechanisms, which respond to perturbations via local activation of specific signalling pathways [39,40]. We hypothesised that pUL21, expressed at late points of infection [4], would likely alter the rate of sphingolipid synthesis and thereby affect lipid-mediated signalling events, rather than altering the overall steady-state lipid composition of infected cells. Synthetic lipids with alkyne-containing acyl chains are efficiently processed by mammalian lipid-modifying enzymes and represent powerful tools to probe lipid metabolism [41]. The impact of pUL21-directed CERT dephosphorylation on sphingolipid metabolism was therefore probed using a clickable analogue of sphingosine (Sph), alkyne-Sph, to monitor the rate of sphingomyelin biogenesis in immortalized human keratinocyte (HaCaT) cells. Exogenous Sph is efficiently incorporated into cellular metabolic pathways, being rapidly converted into ceramide (Cer) and then sphingomyelin (SM) or hexosylceramides (HexCer) like glucosylceramide or galactosylceramide [42]. It is also converted into phosphatidylcholine (PC) via a so-called ‘salvage’ pathway (Fig 1A) that directs sphingosine to palmitoyl-CoA which serves as substrate for re-acetylation of lysophosphatidylcholine [43].

To monitor Sph metabolism, HaCaT cells, either parental or stably expressing pUL21 (HaCaT21), were incubated with alkyne-Sph for five minutes (pulse) and the rate of alkyne-Sph incorporation into the competing metabolic pathways was monitored for two hours (chase) by high performance thin layer chromatography (HPTLC) separation and detection of lipids conjugated to coumarin-azide via a ‘click’ reaction (Fig 1B and 1C). Alkyne-Sph was very efficiently converted to alkyne-Cer in both cell types, the levels of alkyne-Cer remaining relatively stable throughout the chase, and for both cell types synthesis of alkyne-PC and alkyne-SM was observed, but not synthesis of alkyne-HexCer. HaCaT21 cells exhibited substantially reduced rates of alkyne-Sph conversion and reduced alkyne-PC synthesis, with the steady-state level of alkyne-Cer also being reduced. These results indicated that lipid metabolism is altered in HaCaT cells constitutively expressing pUL21. However, it remained unclear whether these differences reflected adaptations of cellular lipid metabolism in response to constitutive pUL21 expression rather than a direct effect upon CERT activity. Since CERT-mediated non-vesicular transport of Cer from the ER to the TGN defines the rate of Cer-to-SM conversion [21–23], pUL21-directed CERT dephosphorylation (and thus activation) should increase the rate of SM synthesis. Consistent with this hypothesis, the abundance alkyne-SM as a fraction of total alkyne-Cer plus alkyne-SM was higher in HaCaT21 versus HaCaT cells at early time points (0–30 min) during the chase (Fig 1D). By the 60 min chase time point the rate of alkyne-SM accumulation slows and the difference in relative abundance between cell lines was diminished, consistent with the alkyne-SM levels in both cell types approaching equilibrium. This increase in alkyne-SM accumulation as a fraction of alkyne-Cer plus alkyne-SM abundance was observed despite lower overall signal for alkyne-SM and alkyne-Cer in HaCaT21 cells when compared to parental cells (Fig 1E). Reduced overall levels of SM plus Cer in HaCaT21 cells likely results from adaptation to constitutive pUL21 expression (and thus constitutive CERT hyperactivation) via stimulation of feedback pathways that reduce Sph to Cer conversion and/or increased back-conversion of SM and/or Cer to Sph. Treatment of HaCaT cells with the highly-specific

147 CERT inhibitor HPA-12 [44] confirmed that the rate of Cer-to-SM conversion was defined by CERT
148 activity: SM synthesis was substantially decreased in HPA-12–treated cells when compared with
149 untreated cells, and there was concomitant accumulation of alkyne-Cer in treated cells (Fig 1B–D).
150 Immunoblot analysis of protein samples that were re-solubilized following their precipitation during lipid
151 extraction (Fig 1F) confirmed that pUL21 was expressed and that dephosphorylated CERT ($CERT^{O}$)
152 predominates in HaCaT21 cells, in contrast to the parental and HPA-12 treated HaCaT cells.

153 pUL21 has multiple functions during infection, promoting the PP1-mediated dephosphorylation of not
154 just CERT but of multiple different cellular and viral proteins [18]. It was therefore essential to identify a
155 point mutant of pUL21 with impaired binding to CERT, but not to other cellular or viral partners, to
156 dissect the functional significance of increased CERT activity during infection. Defining the interaction
157 surfaces of transient protein complexes presents a considerable challenge [45], made more difficult in
158 the case of pUL21 and CERT by their containing multiple domains and regions of intrinsic disorder [18].
159 The minimal region of CERT required for pUL21 binding was thus probed using pull-down experiments
160 where pUL21-GST purified following bacterial expression (bait) was used to capture CERT or
161 truncations thereof (preys) expressed by *in vitro* coupled transcription/translation in wheat germ extract
162 (Fig 2A). The longer cytoplasmic isoform of CERT ($CERT_L$), where expression of exon 11 extends the
163 amino terminal region of the START domain by 26 amino acids ($START_L$), was used since both CERT
164 and $CERT_L$ have been shown to possess ceramide transfer activity [23] and a contribution of these
165 additional 26 amino acids to pUL21 binding could not be excluded. Full-length $CERT_L$ was efficiently
166 captured by pUL21-GST. The PH and $START_L$ domains were also captured by pUL21-GST when
167 expressed individually, albeit less efficiently, suggesting that the $CERT_L$ possesses multiple pUL21-
168 binding motifs. The CERT middle region, MR, was not captured by pUL21-GST and is thus likely to be
169 dispensable for binding. A truncated $CERT_L$ construct that retained the pUL21-binding PH and $START_L$
170 domains, but lacked the majority of the highly flexible MR, was thus designed for use in subsequent
171 biochemical and structural studies (mini$CERT_L$) (Fig 2B). The extent of the MR retained to link the two
172 domains was informed by the crystal structure of the CERT PH:START domain complex [46], defining
173 a minimal distance of at least 55 Å between the PH domain C terminus and the START domain N
174 terminus, and the desire to exclude the predicted coiled-coil region that may cause oligomerisation [26].
175 MR residues 132–350 were thus excluded from mini$CERT_L$. The first 19 amino acids of the PH domain
176 were also omitted from mini$CERT_L$ as this region is predicted to be highly disordered and was excluded
177 in previous structural studies [24,47].

178 Previous studies identified that the MR mediates CERT trimerisation [26,48]. Size-exclusion
179 chromatography with inline multi-angle light scattering (SEC-MALS) (Fig 2C) confirmed that
180 hyperphosphorylated StrepII-tagged $CERT_L^P$, purified following expression in mammalian (Freestyle
181 293F) cells, has an observed mass (184.3 kDa) approaching that expected for a trimer (215.7 kDa).
182 Similarly, a constitutively hypophosphorylated form of $CERT_L$ where S132 is mutated to alanine, and
183 thus cannot become phosphorylated to initiate the SRM phosphorylation cascade [28], had an observed
184 mass (199.2 kDa) approaching that expected for a trimer. In contrast, H_6-mini$CERT_L$ purified following
185 bacterial expression was predominantly monomeric and monodisperse (observed mass 43.9 kDa,

186 expected monomeric mass 44.9 kDa), consistent with trimerization of $CERT_L$ being driven by the MR
187 and not being dependent upon $CERT_L$ phosphorylation.

188 Isothermal titration calorimetry (ITC) demonstrated that pUL21 binds $CERT_L$ with approximately
189 micromolar affinity (Fig 2D,E and Table 1), the observed affinity not differing significantly between the
190 hyperphosphorylated ($CERT_L^P$) and hypophosphorylated ($CERT_L^{S132A}$) forms of the protein. While
191 $CERT_L^{S132A}$ forms a 1:1 complex with pUL21, the observed binding stoichiometry (N) was consistently
192 lower for $CERT_L^P$ (0.74), consistent with a proportion of the pUL21 binding sites on $CERT_L$ being
193 sterically occluded when the protein is hyperphosphorylated. Mini$CERT_L$ and pUL21 form an equimolar
194 complex, binding with micromolar affinity similar to the full-length protein (Fig 2F; Table 1). However,
195 the thermodynamics of binding differ significantly; whereas pUL21 binding to $CERT_L$ is endothermic
196 and entropically driven, binding to mini$CERT_L$ is exothermic and enthalpically driven with minimal
197 change in overall entropy (Table 1). This is consistent with $CERT_L$ undergoing significant conformational
198 rearrangement upon binding to pUL21, whereas the conformational changes to mini$CERT_L$ (if any) upon
199 pUL21 binding are likely to be much more modest.

200 Small-angle X-ray scattering (SAXS) in batch mode was used to probe the solution structure of H_6-
201 mini$CERT_L$ (Fig 2G; Table S1). The frequency distribution of real-space distances ($p(r)$ profile) is largely
202 symmetric (Fig 2H) and the dimensionless Kratky plot (Fig 2I) has a bell-shaped peak at $sR_g = \sqrt{3}$,
203 consistent with mini$CERT_L$ having a compact globular conformation in solution. *Ab initio* modelling of
204 the H_6-mini$CERT_L$ scattering profile using GASBOR [49] yields a dummy-residue model (Fig 2J,K) that
205 closely resembles the crystal structure of CERT START and PH domain complex [46]. A pseudo-atomic
206 model of the H_6-mini$CERT_L$ solution structure, generated using the crystal structures of the CERT PH
207 and START domains determined in isolation [24,25] as rigid bodies, closely resembles the crystal
208 structure of the CERT PH:START domain complex (Fig 2L,M). Collectively, the MALS, ITC and SAXS
209 analysis demonstrates that mini$CERT_L$ forms a compact monomeric protein with high affinity for pUL21,
210 representing an excellent tool for structural studies.

211 Structural characterisation via X-ray crystallography and SAXS has revealed pUL21 to comprise two
212 domains joined by a highly flexible linker [18,50,51], and immunoprecipitation experiments mapped
213 CERT binding to the pUL21 C-terminal domain [18]. The C-terminal domain of pUL21 (pUL21C),
214 spanning amino acids 275–535, was expressed with a hexahistidine tag and purified following bacterial
215 expression. In contrast to a previous report [50] we did not observe co-purification of nucleic acid with
216 H_6-pUL21C, the purified protein having an $A_{260/280}$ ratio of ~0.6. SAXS analysis (Fig S1) confirmed that
217 H_6-pUL21C is monomeric and monodisperse, adopting a compact structure in solution that matches
218 the previously determined crystal structure ($\chi^2 = 0.99$, CorMap p = 0.133) [50]. SEC analysis of a pre-
219 formed complex between purified H_6-mini$CERT_L$ and a 1.34-fold molar excess of H_6-pUL21C confirmed
220 that the two proteins form a stable complex (Fig 3A), suitable for structural studies. ITC demonstrated
221 that H_6-pUL21C forms an equimolar complex with H_6-mini$CERT_L$ with a dissociation constant (K_D) of
222 4.3 ± 1.2 μM (Fig 3B; Table 1). The approximately 4-fold reduction in mini$CERT_L$ binding by pUL21C
223 versus full-length pUL21 is consistent with previous immunoprecipitation results, where transfected

224 pUL21C-GFP captured endogenous CERT slightly less efficiently than did pUL21-GFP in HEK293T
225 cells [18]. These ITC experiments confirm that the C-terminal domain of pUL21 is the major determinant
226 of CERT binding.

227 To probe the structural basis of the CERT recruitment by pUL21, a pre-formed complex of H_6-
228 miniCERT$_L$ and H_6-pUL21C was subjected to SEC with inline SAXS measurement (SEC-SAXS, Fig
229 3C). SAXS data were processed by averaging frames with a consistent calculated radius of gyration
230 (R_g) and then subtracting averaged buffer frames to yield the H_6-miniCERT$_L$:H_6-pUL21C complex
231 scattering profile (Fig 3D). The probable frequency of real-space distances ($p(r)$ profile) of the complex
232 is moderately asymmetric (Fig 3E), in contrast to the highly symmetric $p(r)$ profiles of H_6-pUL21C (Fig
233 S1B) or H_6-miniCERT (Fig 2H) alone, suggesting a less spherical particle, and the dimensions of the
234 complex (R_g 3.5 nm, D_{max} 13.6 nm) are substantially larger than for H_6-pUL21C (R_g 2.2 nm, D_{max} 8.5
235 nm) or H_6-miniCERT (R_g 2.7 nm, D_{max} 9.1 nm). The peak of the dimensionless Kratky plot is slightly
236 higher, with its peak away from $sR_g = \sqrt{3}$ (Fig 3F), suggesting some flexibility in the system granted
237 either by modest dissociation of the complex or some mobility of the H_6-miniCERT$_L$ domains with
238 respect to each other and H_6-pUL21C. *Ab initio* modelling using GASBOR indicated an elongated
239 molecule (Fig 3G). While initial pseudo-atomic models of the complex generated using a fixed
240 conformation of H_6-miniCERT$_L$ did not fit the SAXS profile acceptably, allowing the PH and START$_L$
241 domains freedom to move with respect to each other and to H_6-pUL21C yielded three pseudo-atomic
242 models with high-quality fits to the SAXS profile (Fig 3H and Fig S2). In all three top models miniCERT$_L$
243 binds 'end-on' to the pUL21 molecule, forming an ellipsoidal 'rugby ball' like particle. In two of the top
244 three models miniCERT$_L$ binds the 'left wing' of the dragonfly-shaped pUL21C domain [50], whereas in
245 the other it binds the 'right wing' (Fig S2). These models all have a similar overall shape, and thus all
246 explain the SAXS scattering data well, but the relative orientations of H_6-miniCERT$_L$ and H_6-pUL21C
247 differ. All three top models were thus used to design specific pUL21 mutations that might disrupt
248 (mini)CERT binding.

249 Mutations in pUL21C were designed to identify whether miniCERT$_L$ binds the left or right wing of this
250 domain. Amino acids in helix α4 or the subsequent loop of pUL21C were mutated to test binding to the
251 left wing (Fig 3H, Fig S2), whereas amino acids in helices α5 and α9 were used to test binding to the
252 right wing (Fig S2B). Immunoprecipitation experiments in transfected HEK293T cells that had been
253 infected with HSV-1 lacking pUL21 expression (HSV-1 ΔpUL21) demonstrated that 4 of 5 substitution
254 in the left wing of pUL21C (P365D, V368E, R373E and V382E) disrupted the ability of CERT to co-
255 precipitate with pUL21-GFP (Fig 4A), whereas none in the pUL21C right wing disrupted CERT co-
256 precipitation (Fig S2C). These results are consistent with CERT binding the left wing of pUL21C. The
257 proximity of the pUL21C amino terminus to miniCERT$_L$ in these models is also consistent with
258 observations that CERT binding is lost when pUL21C has a bulky N-terminal GFP tag, but retained
259 when the GFP tag is C-terminal [18].

260 Of the pUL21 substitutions that disrupted CERT binding (Fig 4A), V382E appeared to cause the largest
261 decrease in CERT binding while maintaining the ability of pUL21 to co-precipitate its other known

262 binding partners, PP1 [18] and pUL16 [10]. H_6-pUL21^{V382E} was purified following bacterial expression.
263 Differential scanning fluorimetry (a.k.a. Thermofluor) showed pUL21^{V382E} to be well folded as its thermal
264 stability is similar to wild-type H_6-pUL21 (Fig 4B). ITC analysis demonstrated that H_6-pUL21^{V382E} has
265 approximately 8-fold reduced binding affinity for H_6-miniCERT$_L$ when compared to wild-type pUL21 (Fig
266 4C; Table 1). The effect of the V382E substitution upon the ability of pUL21 to promote CERT
267 dephosphorylation, converting CERT^P to CERT^O, was probed using an *in vitro* dephosphorylation assay
268 with all-purified reagents (Fig 4D and E). The dose-dependent acceleration of GST-PP1 mediated
269 CERT dephosphorylation is greater for wild-type pUL21 than pUL21^{V382E}, consistent with the GST-
270 PP1:pUL21^{V382E} complex having lower affinity for the substrate CERT^P.

271 To probe the ability of pUL21^{V382E} to stimulate CERT dephosphorylation during infection, a mutant strain
272 of HSV-1 encoding pUL21^{V382E} was generated using two-step Red recombination [52].
273 Dephosphorylated CERT (CERT^O) is significantly less abundant in HaCaT cells infected with HSV-1
274 expressing pUL21^{V382E} or lacking pUL21 expression (ΔpUL21) when compared to wild-type HSV-1
275 infected cells (Fig 5A,B). In addition to CERT, pUL21 expression reduces the phosphorylation of
276 multiple substrates of the viral kinase pUS3 in HSV-1 infected cells [18], the phosphorylated forms of
277 these substrates being detectable using an antibody that recognises phosphorylated substrates of the
278 cellular kinase Akt [53]. While infection with ΔpUL21 HSV-1 causes a dramatic increase in the
279 abundance of multiple phosphorylated pUS3 substrates, the abundance of these phosphoforms is
280 indistinguishable between wild-type and pUL21^{V382E} HSV-1 (Fig 5A). This confirms that the V382E
281 substitution specifically disrupts CERT dephosphorylation, rather than generally inhibiting the ability of
282 pUL21^{V382E} to recruit PP1 to substrates. Similar changes in CERT dephosphorylation, but not in the
283 dephosphorylation of other pUS3 substrates, are observed when Vero cells are infected with pUL21^{V382E}
284 HSV-1 (Fig S3A,B). Immunocytochemistry confirms that both wild-type and V382E pUL21 have the
285 similar subcellular localisation, being observed predominantly at the nuclear rim of infected Vero cells
286 (Fig 5C).

287 Metabolic labelling was used to monitor the impact of pUL21-mediated CERT dephosphorylation on
288 sphingolipid biogenesis during infection. A pulse-chase experiment was performed where HaCaT cells
289 infected with wild-type or pUL21^{V382E} HSV-1, or mock infected, were incubated for 5 min with alkyne-
290 Sph at 14 hours post-infection (hpi) and its metabolites were monitored for two hours. Strikingly, Cer
291 accumulates and the rate of SM synthesis is dramatically decreased in cells infected with wild-type and
292 pUL21^{V382E} HSV-1 when compared to uninfected cells (Fig 5D). Although a dramatic decrease in the
293 rate of SM synthesis is seen for both wild-type and mutant HSV-1 infection, the defect is significantly
294 larger in cells infected with HSV-1 pUL21^{V382E} (Fig 5E). The overall abundance of SM plus Cer is similar
295 between infected and uninfected cells, suggesting that Cer to SM conversion is specifically impaired
296 rather than influx of click-Sph into the SM biogenesis pathway being defective (Fig 5F). Taken together,
297 this suggests that pUL21-mediated activation of CERT accelerates Cer to SM conversion during
298 infection, albeit from a much lower base than in uninfected cells.

299 Having confirmed that pUL21^{V382E} HSV-1 specifically lacks the ability to stimulate CERT
300 dephosphorylation, and that HSV-1 encoding pUL21^{V382E} has a reduced rate of Cer to SM conversion,
301 the impact of this deficit upon virus replication and spread in cultured cells was assessed. Wild-type
302 and pUL21^{V382E} HSV-1 form similar sized plaques on HaCaT and Vero cells (Fig 6A), suggesting that
303 CERT dephosphorylation is dispensable for efficient viral cell-to-cell spread. A single-step growth curve,
304 where Vero and HaCaT cells are infected at a high multiplicity of infection (MOI) and the production of
305 infectious progeny is monitored over time, was used to compare the replication of wild type and
306 pUL21^{V382E} HSV-1 (Fig 6B). Both viruses produce similar abundance of infectious progeny by 24 hours
307 post infection. However, in two biologically independent experiments performed for each cell type the
308 kinetics of virus replication was consistently accelerated, with higher titres of pUL21^{V382E} HSV-1 being
309 observed between 6–12 hours post-infection.

310 While HSV-1 preferentially remains cell-attached, spreading via direct cell:cell contacts, the cell-free
311 secretion of virions from infected cells is altered when CERT is depleted or overexpressed [54]. Cell-
312 free release of pUL21^{V382E} HSV-1 was determined by quantitating the amount of infectivity secreted into
313 the medium as a percentage of overall infectivity (secreted plus cell-associated), normalised for each
314 independent replicate to the secretion of a wild-type virus in control experiments performed at the same
315 time. HaCaT cells infected for 12 h with various MOI of pUL21^{V382E} HSV-1 did not release significantly
316 more or less infectivity when compared to WT HSV-1 infection (Fig 6C). Similarly, the cell-free release
317 of infectivity at 12 hpi did not differ between Vero cells infected with pUL21^{V382E} or WT HSV-1 (Fig S3C).

318

319 **Discussion**

320 HSV-1 extensively remodels the proteome of infected cells, altering both the abundance [4] and post-
321 translational modification status [2,18,55] of multiple cellular proteins. We know much less about HSV-
322 1 mediated changes to the cellular lipidome, although previous studies have identified that HSV-1
323 infection alters the production of the phospholipid plasmalogen [56], changes phosphoinositide levels
324 [57], and increases the rate of *de novo* phospholipid synthesis [58]. By combining biochemical and
325 structural studies with cell-based models of infection we show here that pUL21 accelerates the
326 conversion of Cer to SM in infected cells by promoting dephosphorylation and activation of the Cer
327 transport protein CERT (Fig 5). This is the first observation of a viral protein directly binding CERT and
328 altering its activity. While pUL21-mediated CERT activation causes a modest increase in the rate of
329 virus replication, it does not contribute significantly to overall yield or cell-to-cell spread of HSV-1 in
330 cultured keratinocytes or epithelial cells (Fig 6).

331 Our previous work showed that pUL21 is a phosphatase adaptor with multiple different targets [18].
332 Mutation of the pUL21 TROPPO motif, required for PP1 binding and thus stimulation of
333 dephosphorylation, dramatically reduced the replication and spread of HSV-1. While the TROPPO motif
334 was identified via its conservation across alphaherpesvirus sequences, the molecular basis of CERT
335 recruitment remained unknown. Biochemical mapping and SAXS structural characterisation allowed us
336 to identify a specific mutation, V382E, that decreases the affinity of pUL21 for miniCERT$_L$ by
337 approximately 8-fold (Fig 4C). While this reduction in affinity is moderate when assayed in dilute
338 biochemical solution, it is sufficient to disrupt co-precipitation of CERT from transfected cells (Fig 4A),
339 it abolishes pUL21-mediated dephosphorylation of CERT during infection (Fig 5A,B), and it significantly
340 increases the rate of Cer to SM conversion (Fig 5E). These results are consistent with other binding
341 partners competing to bind CERT and/or pUL21 within the context of infected cells, these competing
342 interactions amplifying the effect of reduced pUL21:CERT binding affinities. The V382E mutation does
343 not prevent pUL21 binding to pUL16 (Fig 4A) nor its ability to stimulate dephosphorylation of other
344 targets (Fig 5A), confirming that pUL21 binds CERT via a molecular surface that is distinct from the
345 binding site(s) of other targets. The wild-type levels of virus replication and cell-to-cell spread observed
346 for pUL21^{V382E} HSV-1 are consistent with our previous *in vitro* evolution studies of HSV-1 mutants where
347 the pUL21 TROPPO motif was mutated [18]. Adaptation of the virus to the loss of pUL21 PP1 binding,
348 via suppressor mutations that reduce the activity of the kinase pUS3, restored virus replication and
349 spread without restoring enhanced CERT dephosphorylation [18]. We therefore conclude CERT is not
350 a critical substrate of pUL21 for virus replication and spread in cultured fibroblasts and keratinocytes.
351 However, we note that HSV-1 is a neurotropic virus and that sphingolipids like SM are highly enriched
352 in neurons, where they are critical for correct neuronal development and function [31]. Studying the role
353 of pUL21-mediated CERT dephosphorylation in neurons thus remains an important question for future
354 investigation.

355 Studies of cellular lipid metabolism are complicated by robust cellular feedback mechanisms [59] and
356 challenges in accurately detecting changes in lipid abundance [60]. Here, we successfully employed

357 lipid labelling, click chemistry and HPTLC to monitor the kinetics of sphingosine metabolism, revealing
358 that HSV-1 pUL21 significantly increases the rate of CERT-mediated Cer to SM conversion both outside
359 (Fig 1) and within (Fig 5) the context of infection. Furthermore, we observe a striking increase in the
360 abundance of labelled Cer when cells are infected with HSV-1, this increase being greater when pUL21-
361 mediated CERT activation has been abolished. The dramatic change in the rate of Cer to SM
362 conversion is most likely explained by the known propensity of HSV-1 to promote dispersal of the Golgi
363 and TGN [5,61]. Such dispersal would alter ER:TGN contact sites, where CERT-mediated transport
364 enables Cer to SM conversion by TGN-resident sphingomyelin synthase [62].

365 HSV-1 utilizes the PKD-mediated trafficking from the TGN to the plasma membrane [63]. Disruption of
366 PKD-mediated trafficking has been shown to alter virus secretion, with siRNA-mediated depletion of
367 CERT increasing the secretion of extracellular (cell-free) HSV-1 particles and CERT overexpression
368 reducing virus secretion [54]. We do not observe changes in the secretion of pUL21^{V382E} HSV-1, which
369 lacks the ability to dephosphorylate CERT and thus activate CERT-mediated Cer transport. While these
370 results may appear at first glance to be contradictory, it should be noted that in our experiments the
371 cells contained wild-type levels of CERT and cells infected with either ΔpUL21 or pUL21^{V382E} HSV-1
372 have similar levels of active (CERT^{P}) and inactive (CERT^{O}) protein compared to uninfected controls
373 (Fig 5A). In contrast, siRNA depletion would lead to a complete absence of CERT and of CERT-
374 mediated lipid transfer. Furthermore, the previous study demonstrated that treatment of infected cells
375 with HPA-12 did not stimulate virus particle secretion [54]. This insensitivity of HSV-1 secretion to CERT
376 pharmacological inhibition, combined with our observation that pUL21-mediated CERT activation does
377 not alter HSV-1 secretion, strongly suggests that CERT catalytic activity is not directly linked to the
378 regulation of virus secretion.

379 Our observation of labelled Cer accumulation during HSV-1 infection (Fig 5) is consistent with an earlier
380 report that HSV-1 infection causes an approximately 2-fold increase in Cer abundance within BHK-21
381 cells [34]. Cer has many distinctive physical properties that set it apart from other membrane lipids: it
382 has negative intrinsic curvature, it increases the order of phospholipids in membranes, and it makes
383 biological membranes more permeable to even large solutes such as proteins [64]. Nascent HSV-1
384 particles must traverse multiple biological membranes during virus assembly, most notably during
385 capsid egress from the nucleus. Being too large to egress via nuclear pores, capsids leave by budding
386 into and then out of the perinuclear space, the former step being catalysed by the herpesvirus nuclear
387 egress complex (NEC) [65]. A recent study identified that the NEC induces lipid ordering to generate
388 the negative curvature required for capsid budding [66]. It is tempting to speculate that the accelerated
389 replication kinetics of pUL21^{V382E} HSV-1 arises, at least in part, from an increased rate of nuclear capsid
390 egress owing to increased Cer abundance. This effect would be distinct from the previously
391 demonstrated role of pUL21 in promoting nuclear egress via regulating the phosphorylation of NEC
392 components [18,20]. Increased Cer abundance could also stimulate secondary envelopment of virus
393 particles at post-Golgi membranes. However, in addition to potentially promoting virus assembly,
394 accumulation of Cer can lead to caspase 3 activation and apoptosis via increased mitochondrial outer
395 membrane permeabilization [67], and HSV-1 is known to encode proteins that defend against ceramide-

396 induced apoptosis [68]. It is therefore possible that pUL21-stimulated acceleration of Cer to SM
397 conversion acts to limit the pro-apoptotic activity of Cer, although confirmation of this requires further
398 study.

399 In summary, we demonstrated that pUL21 dephosphorylates and activates the cellular lipid transport
400 protein CERT, stimulating conversion of Cer to SM. Characterising the solution structure in complex
401 with the PH and START domains of CERT allowed us to identify a single amino acid mutation of pUL21
402 that disrupts CERT dephosphorylation in infected cells. HSV-1 encoding this pUL21 mutant had
403 accelerated replication kinetics but otherwise resulted in similar virus yields and plaque sizes,
404 confirming that pUL21-mediated dephosphorylation of other cellular and/or viral targets underpin its role
405 in HSV-1 replication and spread. The functional rationale for pUL21-mediated modulation of CERT
406 activity by HSV-1 remains elusive, but we have defined the molecular tools that will allow its dissection
407 in other cell types and/or animal models of infection.

408

409 **Materials and methods**

410 *Plasmids*

411 The StrepII-CERT transient mammalian expression construct was described previously [18]. For
412 generation of stable cells, a synthetic gene encoding human $CERT_L$ (UniProt Q9Y5P4-1) was cloned
413 into a modified version of plasmid PB-T [69] that encodes an N-terminal StrepII tag and a woodchuck
414 hepatitis virus posttranscriptional regulatory element [70] in the 3′ untranslated region. The S132A
415 substitution was introduced into this vector using QuikChange mutagenesis (Agilent) according to the
416 manufacturer's instructions. $CERT_L$ destined for expression using *in vitro* transcription/translation
417 system from wheat germ extract was cloned into the plasmid pF3A WG BYDV (Promega) with an N-
418 terminal myc epitope tag. The truncations of $CERT_L$ were generated by inverse PCR (MR, residues
419 123–364; $START_L$, residues 365–624) or by introduction of a stop codon (PH, residues 1–122) using
420 QuikChange mutagenesis. For purification following bacterial expression, $miniCERT_L$ (residues 20–131
421 plus 351–624) was cloned into pOPTH [71], encoding a N-terminal MAH_6 tag. The generation of pUL21-
422 H_6 and pUL21-GFP were described previously [18] and single amino acid substitutions were introduced
423 by QuikChange mutagenesis. pUL21-H_6 was subcloned into pOPTH and inverse PCR was used to
424 generate H_6-pUL21C, encoding pUL21 amino acids 275–535. A plasmid (UK622) encoding mouse
425 PP1γ (UniProt P63087) with an N-terminal GST tag [72] was a kind gift from David Ron (Cambridge
426 Institute for Medical Research). To generate $pUL21^{V382E}$ HSV-1, pEPkan-S containing an I-SceI/KanR
427 selection cassette was used [52].

428 *Mammalian cell culture*

429 Mycoplasma-free spontaneously immortalised human keratinocyte (HaCaT) cells [73], HaCaT cells
430 stably expressing pUL21 (HaCaT21) [18], African green monkey kidney (Vero) cells (ATCC #CRL-
431 1586) and human embryonic kidney (HEK)293T cells (ATCC #CRL-3216) were maintained in
432 Dulbecco's Modified Eagle Medium with high glucose (Merck), supplemented with 10% (v/v) heat-
433 inactivated foetal calf serum (FCS) and 2 mM L-glutamine (complete DMEM) in a humidified 5% CO_2
434 atmosphere at 37°C. For protein purification, Freestyle 293F suspension cells (ThermoFisher) were
435 grown in Freestyle 293F medium (Gibco) on a shaking platform (125 rpm) in a humidified 8% CO_2
436 atmosphere at 37°C.

437 Doxycycline-inducible stably transfected Freestyle 293F cells expressing StrepII-$CERT_L$ and StrepII-
438 $CERT_L^{S132A}$ were generated using a piggyBac transposon-based system [69]. A 30 mL suspension
439 culture of Freestyle 293F cells at 1×10^6 cells/mL were transfected with a 5:1:1 mass ratio of PB-T-
440 $CERT_L^{(S132A)}$:PB-RN:PBase (35 µg total DNA) using Freestyle MAX transfection reagent (Invitrogen) as
441 per the manufacturer's instructions. After two days the cells were transferred to fresh media
442 supplemented with 500 µg/mL Geneticin (Gibco) and the drug selection was continued for two weeks
443 with media replenishment every three days.

444 *GFP affinity capture*

445 Monolayers of HEK293T cells grown in 9 cm dishes were transfected with TransIT-LT1 (Mirus) using
446 7.7 µg of pEGFP-N1 (for GFP alone), pUL21-GFP, or point mutants thereof, following the
447 manufacturer's instructions. At 24 hours post-transfection, the cells were harvested by scraping into the
448 medium, pelleted (220 g, 5 min, 4°C), washed three times with cold phosphate buffered saline (PBS)
449 and lysed at 4°C in 1 mL lysis buffer (10 mM Tris pH 7.5, 150 mM NaCl, 0.5 mM EDTA, 0.5% NP-40,
450 1:100 diluted EDTA-free protease inhibitor cocktail [Merck]) for 45 min before clarification (21,000×g,
451 10 min, 4°C). After immunoprecipitation with GFP-Trap beads (ChromoTek) performed in accordance
452 with the manufacturer's protocol, the samples were eluted by incubation at 95°C for 5 min in 45 µL 2×
453 SDS-PAGE loading buffer. Input and bound samples were separated by SDS-PAGE and analysed by
454 immunoblot.

455 *GST pulldown*

456 GST pulldown experiments were carried out in 96-well flat-bottomed plates (Greiner) using magnetic
457 glutathione beads (Thermo Scientific) to capture the GST-tagged pUL21 (bait protein). First, 0.5 nmol
458 of purified bait protein was incubated with the beads at 4°C for 30 min. The beads were washed three
459 times with wash buffer (20 mM Tris pH 8.5, 200 mM NaCl, 0.1% NP-40, 1 mM DTT, and 1 mM EDTA),
460 then incubated at 4°C for 60 min with various truncations of myc-CERT$_L$ (prey proteins), expressed
461 using the TNT SP6 High Yield Wheat Germ *in vitro* transcription/translation system (Promega) in
462 accordance with the manufacturer's protocol, followed by four washes in wash buffer. Protein was
463 eluted using wash buffer supplemented with 50 mM reduced glutathione before being analysed by SDS-
464 PAGE and immunoblotting.

465 *Antibodies*

466 The following antibodies with listed dilutions were used for immunoblotting: rabbit anti-CERT 1:10,000
467 (Abcam, ab72536), mouse anti-pUL21 1:50 [1F10-D12] [18] for Fig 1F [note: this monoclonal antibody
468 does not recognize pUL21^{V382E}], rabbit anti-pUL21 1:5000 [10] for Fig 5A and S2A, mouse anti-GAPDH
469 1:10,000 (GeneTex, GTX28245), mouse anti-Myc 1:4000 (Millipore, 05-724), mouse anti-PP1α 1:1000
470 (Santa Cruz, sc-271762), rabbit anti-pUL16 1:2000 [74], mouse anti-VP5 1:50 [DM165] [75], rabbit anti-
471 phospho-Akt substrates 1:1000 (Cell Signalling, 9611). Fluorescently labelled secondary antibodies
472 were used at 1:10,000 dilution: LI-COR IRDye 680T donkey anti-rabbit (926–68023) and goat anti-
473 mouse (926–68020), LI-COR IRDye 800CW conjugated donkey anti-rabbit (926–32213) and goat anti-
474 mouse (926–32210). For immunocytochemistry, mouse anti-pUL21 1:1 [L1E4-C10], which was
475 generated in the same immunisation experiments as anti-pUL21 [1F10-D12] [18], and Alexa Fluor 488
476 conjugated goat anti-mouse 1:1000 (Invitrogen, A21236) were used. For visualising HSV-1 plaques
477 mouse anti-gD (LP2) 1:50 [76] and HRP-conjugated rabbit anti-mouse 1:5000 (DaKo, P0161) were
478 used.

479 *Recombinant protein purification following bacterial expression*

480 All recombinant proteins were expressed in *Escherichia coli* T7 Express *lysY/I*^{q} cells (New England
481 Biolabs). Except for GST-PP1γ, cells were grown in 2×TY medium at 37°C to an OD_{600} of 0.8–1.2 before
482 cooling to 22°C and inducing protein expression by addition of 0.4 mM isopropyl β-D-
483 thiogalactopyranoside (IPTG). At 16–20 h post-induction, cells were harvested by centrifugation and
484 pellets were stored at -70°C until required. For GST-PP1γ, the 2×TY medium was supplemented with
485 1 mM $MnCl_2$ and the cultures were cooled to 18°C upon reaching an OD_{600} of 0.8, followed by induction
486 using 1 mM IPTG. For all recombinant proteins, cells were resuspended in lysis buffer (see below) at
487 4°C before lysis using a TS series cell disruptor (Constant Systems) at 24 kpsi. Lysates were cleared
488 by centrifugation (40,000×g, 30 min, 4°C) and incubated with the relevant affinity resins for 1 h at 4°C
489 before extensive washing (≥ 20 column volumes) and elution using the relevant elution buffer (see
490 below). Samples were concentrated and subjected to size exclusion chromatography (SEC, see below).
491 Fractions containing the desired protein as assessed by SDS-PAGE were pooled, concentrated, snap-
492 frozen in liquid nitrogen and stored at -70°C.

493 The lysis buffer for pUL21-GST (20 mM Tris pH 8.5, 300 mM NaCl, 0.5 mM $MgCl_2$, 1.4 mM β-
494 mercaptoethanol, 0.05% TWEEN-20) and GST-PP1γ (50 mM Tris pH 7.5, 500 mM NaCl, 1 mM $MnCl_2$,
495 0.5 mM $MgCl_2$, 1.4 mM β-mercaptoethanol, 0.05% TWEEN-20) was supplemented with 200–400 U
496 bovine DNase I (Merck) and 200 µL EDTA-free protease inhibitor cocktail (Merck). Cleared lysates were
497 incubated with glutathione Sepharose 4B (Cytiva), washed with wash buffer (20 mM Tris pH 8.5 [pUL21-
498 GST] or 7.5 [GST-PP1γ], 500 mM NaCl, 1 mM DTT, plus 1 mM $MnCl_2$ [GST-PP1γ only]) and the proteins
499 eluted using wash buffer supplemented with 25 mM reduced glutathione. SEC was performed using a
500 HiLoad Superdex S200 16/600 column (Cytiva) equilibrated in 20 mM Tris pH 8.5, 500 mM NaCl, 1 mM
501 DTT (pUL21-GST) or 50 mM Tris pH 7.5, 100 mM NaCl, 1 mM DTT (GST-PP1γ).

502 pUL21-H_6, pUL21^{V382E}-H_6 and H_6-pUL21C were purified in Tris buffer at pH 8.5 in with 500 mM NaCl
503 and H_6-miniCERT$_L$ was purified in Tris buffer at pH 7.5 with 150 mM NaCl. Lysis buffer (20 mM Tris, 20
504 mM imidazole, NaCl, 0.5 mM $MgCl_2$, 1.4 mM β-mercaptoethanol, 0.05% TWEEN-20) was
505 supplemented with 200–400 U bovine DNase I (Merck) and 200 µL EDTA-free protease inhibitor
506 cocktail (Merck). Cleared lysates were incubated with Ni-NTA agarose (Qiagen), washed with wash
507 buffer (20 mM Tris, 20 mM imidazole, NaCl) and eluted using elution buffer (20 mM Tris, 250 mM
508 imidazole, NaCl) SEC was performed using a HiLoad Superdex S200 column (Cytiva) equilibrated in
509 20 mM Tris, NaCl, 1 mM DTT.

510 *Recombinant protein purification following mammalian cell expression*

511 StrepII-CERT^{P} used for phosphatase assays was purified following transient transfection of Freestyle
512 293F cells, as described before [18]. StrepII-CERT$_L^{P}$ and StrepII-CERT$_L^{S132A}$ were purified from stably
513 transfected Freestyle 293F cells following induction with 2 µg/mL doxycycline (Fisher) for 72 hours.
514 Next, cells were harvested by centrifugation (220×g, 5 min, 4°C) and washed once with ice-cold PBS

515 before being resuspended in ice-cold lysis buffer with phosphatase inhibitors [StrepII-CERT$_L^P$ only] (100
516 mM Tris pH 8.0, 150 mM NaCl, 0.5 mM EDTA, 1 mM DTT, [10 mM tetrasodium pyrophosphate, 100
517 mM NaF, 17.5 mM β-glycerophosphate]). Cells were lysed by passage through a 23G needle six times
518 and lysates were clarified by centrifugation (40,000 g, 30 min, 4°C). The supernatants were sonicated
519 at 50% amplitude for 60 s using a sonicating probe (MSE) and the supernatants were passed through
520 a 0.45 µm syringe filter (Sartorius). StrepII-tagged proteins were captured using 1 mL StrepTrap HP
521 column (Cytiva) that had been pre-equilibrated in wash buffer (100 mM Tris pH 8.0, 150 mM NaCl, 0.5
522 mM EDTA, 1 mM DTT). After extensive washing (20 column volumes) the protein was eluted using
523 wash buffer supplemented with 2.5 mM desthiobiotin. Pooled eluate was applied to a Superose 6
524 10/300 GL column (Cytiva) column equilibrated in ITC buffer (20 mM Tris pH 8.5, 500 mM NaCl, 0.5
525 mM Tris(2-carboxyethyl)phosphine [TCEP]) and fractions containing StrepII-CERT$_L$ as assessed by
526 SDS-PAGE were pooled, concentrated and used for downstream applications.

527 *Mutagenesis of viral genomes and generation of recombinant HSV-1*

528 All HSV-1 strain KOS viruses used in this study were reconstituted from a bacterial artificial
529 chromosome (BAC) [77] and the mutated strain was generated using the two-step Red recombination
530 method [52] with the following primers:

531 Forward: 5′-CGGCTCGTAGGCCGGTACACACAGCGCCACGGCCTGTACG**AA**CC
532 TCGGCCCGACGACCCAGTAGGATGACGACGATAAGTAGGG

533 Reverse: 5′-CGTTGATGGCATCGGCCAAGACTGGGTCGTCGGGCCGAGG**TT**CG
534 TACAGGCCGTGGCGCTGTCAACCAATTAACCAATTCTGATTAG

535 The generation of pUL21 deletion mutant (ΔpUL21) was described previously [18]. To generate the P0
536 stocks, Vero cells were transfected with the recombinant BAC DNA together with pGS403 encoding
537 Cre recombinase (to excise the BAC cassette) using TransIt-LT1 (Mirus) following the manufacturer's
538 instructions. After 3 days the cells were scraped into the media, sonicated at 50% power for 30 s in a
539 cup-horn sonicator (Branson), and titrated on Vero cell monolayers. The subsequent stocks were
540 generated by infecting either Vero (HSV-1 WT) or HaCaT pUL21 cells (HSV-1 mutants) at MOI of 0.01
541 for 3 days. The cells were then scraped and isolated by centrifugation at 1,000×g for 5 min. Pellets were
542 resuspended in 1 mL of complete DMEM supplemented with 100 U/mL penicillin, 100 µg/mL
543 streptomycin and freeze/thawed thrice at -70°C before being aliquoted, titered on Vero cell monolayers,
544 and stored at -70°C until required. The presence of the desired mutation in the reconstituted virus
545 genomes was confirmed by sequencing the pUL21 gene.

546 *Metabolic labelling and lipid extraction for thin layer chromatography*

547 Metabolic labelling was performed using sub-confluent (60–80% confluence) HaCaT or HaCaT21 cells
548 grown in a 6-well plate. For analysis of stable cell lines, the cells were pre-treated for 30 min with
549 complete DMEM containing 1 µM N-(3-Hydroxy-1-hydroxymethyl-3-phenylpropyl)dodecanamide (HPA-

550 12, Tokyo Chemical Industry) dissolved in 0.1% dimethyl sulfoxide (DMSO, Merck), or 0.1% DMSO
551 alone, and HPA-12 or DMSO were retained at the same concentrations throughout the subsequent
552 incubation steps. For infection, cells were infected (below) 14 hours before metabolic labelling.

553 For metabolic labelling, wells were washed twice with warm PBS before incubation in 500 µL pre-
554 warmed DMEM with 1% (v/v) Nutridoma (Merck) supplemented with 5 µM clickable sphingosine
555 (Cayman Chemical) for 5 min (pulse). Next, cells were washed twice with warm PBS and 1 mL of pre-
556 warmed DMEM with 1% (v/v) Nutridoma was added to each well, followed by incubation at 37°C for the
557 indicated times of chase. Click-Sph was stored as a 3.3 mM ethanolic stock solution at -20°C.

558 At the indicated times of chase, the plate with cells was transferred onto the ice, washed twice with 1
559 mL ice-cold PBS, scraped into 300 µL of ice-cold PBS and transferred into appropriate 1.5 mL
560 microcentrifuge tubes containing 600 µL of methanol. To each tube 150 µL of chloroform was added,
561 followed by vigorous vortexing. The precipitated protein was pelleted (20,000×g, 1 min) at room
562 temperature (RT). The organic supernatant was transferred to separate 2 mL tubes containing 300 µL
563 chloroform. 600 µL of 0.1% acetic acid in H_2O was subsequently added to each tube to induce formation
564 of two phases. Following extensive vortexing, the phases were separated by centrifugation (20,000×g,
565 1 min, RT) and the lower phase was transferred to a new 1.5 mL microcentrifuge tube. This lipid-
566 containing solvent phase was dried in a UniVapo centrifugal vacuum concentrator (UniEquip) at 30°C
567 for 20 min.

568 If required for SDS-PAGE analysis, the protein pellet was solubilized with 5 µL 10% (w/v) SDS, diluted
569 in 75 µL lysis buffer (20 mM Tris 7.5, 150 mM NaCl, 1% (v/v) Triton X-100), boiled for 10 min and
570 sonicated at 75% power for 60 s in a cup-horn sonicator (Branson). The protein samples were mixed
571 with 5× loading buffer before being subjected to SDS-PAGE analysis.

572 *Click reaction and thin layer chromatography of labelled lipids*

573 Lipid standards (16:0(Alkyne)-18:1 PC [Avanti], pacFA GalCer [Avanti], d18:1(Alkyne)-6:0 Cer [Cayman
574 Chemicals], 18:0(Alkyne) Sph [Cayman Chemicals]) or extracted lipids (above) were resuspended in
575 20 µL of 1:1 chloroform:ethanol. To each tube 1 µL of Tris((1-benzyl-4-triazolyl)methyl)amine (TBTA)
576 solution (2.5 mM in DMSO; Merck), 10 µL of Tetrakis(acetonitrile)copper(I) tetrafluoroborate (10 mM in
577 acetonitrile; Merck) and 1 µL of 3-azido-7-hydroxycoumarin solution (1 mM in EtOH; Jena Bioscience)
578 was added. After brief mixing, the reaction was dried in a UniVapo centrifugal vacuum concentrator
579 (UniEquip) for 10 min at 45°C. Lipids were dissolved in 20 µL of 65:25:4:1
580 chloroform:methanol:water:acetic acid, of which 8 µL was spotted on a 20×10 cm HPTLC Silica gel 60
581 plates (Merck). When dried, the plate was developed for 5 cm with 65:25:4:1
582 chloroform:methanol:water:acetic acid, dried again and developed for 9 cm with 1:1
583 hexane:ethylacetate. Labelled lipids were visualized via UV illumination using a G:BOX Chemi XX9
584 (Syngene) and bands were quantified using the Image Studio Lite software (LI-COR) with local
585 background subtraction.

586 *Virus infections*

587 Monolayers of indicated cells were infected by overlaying with the appropriate viruses, diluted in
588 complete DMEM to the specified MOI. The time of addition was designated 0 hours post-infection (hpi).
589 Cells were incubated with the inoculum at 37°C in a humidified 5% CO_2 atmosphere for 1 hour, rocking
590 the tissue culture plate housing the monolayers every 15 min, before complete DMEM supplemented
591 with 100 U/mL penicillin, 100 µg/mL streptomycin was added to dilute the original infection medium five-
592 fold. Infected cells were incubated at 37°C in a humidified 5% CO_2 atmosphere and harvested at the
593 specified times.

594 *Immunoblotting*

595 For analysis of protein expression and phosphorylation, cells were washed two times with ice-cold 50
596 mM Tris pH 8.5, 150 mM NaCl and scraped into 100 µL of ice-cold lysis buffer (50 mM Tris pH 8.5,
597 150mM NaCl, 1% (v/v) Triton-X100, 1% (v/v) EDTA-free protease inhibitor cocktail [Merck], 10 mM
598 tetrasodium pyrophosphate, 100 mM NaF and 17.5 mM β-glycerophosphate). After 30 min incubation
599 on ice, the lysates were sonicated (two 15 s pulses at 50% power) in a cup-horn sonicator (Branson)
600 followed by centrifugation at 20,000×g for 10 min. For all samples, protein concentrations were
601 determined using a BCA assay (Peirce) and normalized protein lysates were analysed by SDS-PAGE.
602 For enhanced separation of phosphorylated proteins, 7% (w/v) acrylamide gels contained 50 µM $MnCl_2$
603 and 25 µM PhosTag reagent (Wako) where indicated. Separated proteins were then transferred to
604 nitrocellulose membranes using the Mini-PROTEAN system (Bio-Rad) and analysed by
605 immunoblotting, signals being detected using Odyssey CLx Imaging System (LI-COR). For quantitation
606 of CERT phosphoform relative abundance, the signal for $CERT^O$ band alone and for all CERT bands
607 ($CERT^O$ + $CERT^P$) were quantitated using Image Studio Lite software (LI-COR) with local background
608 subtraction.

609 *Analytical SEC of miniCERT$_L$:pUL21C complex*

610 Analytical SEC experiments were performed using Superdex 200 10/300 GL (Cytiva) column
611 equilibrated in 20 mM Tris pH 8.5, 500 mM NaCl, 1 mM DTT. To allow complex formation, 200 µL of
612 140 µM H_6-miniCERT$_L$ and 680 µL of 55.4 µM H_6-pUL21C were mixed and incubated for 15 min at room
613 temperature prior to injection.

614 *Isothermal titration calorimetry (ITC)*

615 ITC experiments were performed at 25°C using an MicroCal PEAQ-ITC automated calorimeter (Malvern
616 Panalytical). Proteins were transferred into ITC buffer (20 mM Tris pH 8.5, 500 mM NaCl, 0.5 mM TCEP)
617 either by SEC or extensive dialysis prior to experiments. Titrants (StrepII-CERT$_L^P$ at 192–328 µM,
618 StrepII-CERT$_L^{S132A}$ at 196–334 µM or H_6-miniCERT$_L$ at 195–376 µM) were titrated into titrates (pUL21-
619 H_6 at 20–33 µM, pUL21^{V382E}-H_6 at 19.5–32 µM or H_6-pUL21C at 30–32.5 µM) using either 19×2 µL or

620 12×3 µL injections. Data were analysed using the MicroCal PEAQ-ITC analysis software (Malvern
621 Panalytical) and fitted using a one-site binding model.

622 *Multi-angle light scattering (MALS)*

623 MALS data were collected immediately following SEC (SEC-MALS) by inline measurement of static
624 light scattering (DAWN 8+; Wyatt Technology), differential refractive index (Optilab T-rEX; Wyatt
625 Technology), and UV absorbance (1260 UV; Agilent Technologies). Samples (100 µL) were injected
626 onto an Superose 6 increase 10/300 GL column (Cytiva) equilibrated in in 20 mM Tris pH 8.5, 500 mM
627 NaCl, 0.5 mM TCEP at 0.4 mL/min. The protein samples were injected at the concentration of 2 mg/mL.
628 Molecular masses were calculated using ASTRA 6 (Wyatt Technology) using a protein dn/dc of
629 0.186 mL/g.

630 *Small-angle X-ray scattering (SAXS)*

631 SAXS experiments were performed in batch mode (H_6-pUL21C and H_6-miniCERT$_L$) or inline following
632 SEC (H_6-pUL21C:H_6-miniCERT$_L$) at EMBL-P12 bioSAXS beam line (PETRAIII, DESY, Hamburg,
633 Germany) [78,79].

634 For SAXS in batch mode, scattering data ($I(s)$ versus s, where $s = 4\pi\sin\theta/\lambda$ nm^{-1}, 2θ is the scattering
635 angle, and λ is the X-ray wavelength, 0.124 nm) were collected from the indicated batch samples and
636 a corresponding solvent blank (20 mM Tris pH 8.5, 500 mM NaCl, 3% (v/v) glycerol, 1 mM DTT). The
637 scattering profiles of H_6-miniCERT$_L$ (1.73, 2.59, 3.46 and 6.91 mg/mL) and H_6-pUL21C (0.76 mg/mL)
638 were measured in continuous-flow mode using an automated sample changer (30 µL sample at 20°C;
639 1 mm pathlength). The sample and buffer measurements were measured as 100 ms data frames on a
640 Pilatus 6M area detector for total exposure times of 2.1 and 2.6 s, respectively. For H_6-miniCERT$_L$, the
641 resulting SAXS curves were extrapolated to infinite dilution.

642 For SEC-SAXS experiments, the scattering data were recorded using a Pilatus 6M detector (Dectris)
643 with 1 s sample exposure times for a total of 3600 data frames spanning the entire course of the SEC
644 separation. Proteins were mixed at 1:1 molar ratio, incubated on ice for 15 min, and then concentrated
645 using a centrifugal concentrator to the desired concentration as estimated from absorbance using
646 extinction coefficients [80] calculated assuming a 1:1 molar ratio. 40 µL of purified H_6-pUL21C:H_6-
647 miniCERT$_L$ (4.3 mg/mL) was injected at 0.35 mL/min onto an Superdex 200 Increase 5/150 GL column
648 (Cytiva) equilibrated in 20 mM Tris pH 8.5, 500 mM NaCl, 3% (v/v) glycerol, 1 mM DTT. SAXS data
649 were recorded from a single peak (frames 1245–1296 s) and solvent blank was collected from pre-
650 elution frames (frames 247–411). Primary data reduction was carried out using CHROMIXS [81] and
651 2D-to-1D radial averaging was performed using the SASFLOW pipeline [82]. Processing and analysis
652 of the SAXS output was performed using the ATSAS 3.0.2 software package [83]. The extrapolated
653 forward scattering intensity at zero angle, $I(0)$, and the radius of gyration, R_g, were calculated from the
654 Guinier approximation ($\ln I(s)$ vs s^2, for $sR_g < 1.3$). The maximum particle dimension, D_{max}, was estimated

655 based on the probable distribution of real-space distances *p*(*r*) which was calculated using GNOM [84].
656 A concentration-independent estimate of molecular weight was determined using a Bayesian
657 consensus method [85]. All structural parameters are reported in Table S1.

658 *Ab initio* modelling was performed using GASBOR [49] and figures show the models that best fit their
659 corresponding SAXS profiles (lowest χ^2). Pseudo-atomic modelling was performed using CORAL [86].
660 For H_6-miniCERT$_L$, crystal structures of the CERT PH (PDB ID 4HHV) [24] and START (PDB ID 2E3M)
661 [25] domains were used, the latter including predicted secondary structure as modelled by I-TASSER
662 [87] for intron 11 (residues 371-396), present only in CERT$_L$. The miniCERT$_L$ 23 amino acid linker and
663 the purification tag (MAH_6) were modelled using CORAL. The model with the best fit was superimposed
664 onto the PH:START crystal structure (PDB ID 5JJD) [46] by aligning the START domains using PyMOL
665 version 2.5.2 (Schrödinger). For H_6-pUL21C, the N-terminal (MAH_6QD) and C-terminal (HGQSV)
666 elements missing from the crystal structure (PDB ID 5ED7) [50] were modelled using CORAL. For H_6-
667 pUL21C:H_6-miniCERT$_L$, the heterodimer was modelled using the SAXS curve of the complex using a
668 fixed conformation of H_6-pUL21C and mobile CERT domains, with unstructured elements modelled as
669 above. All the models were assessed for fit to the corresponding SAXS profiles (χ^2 and CorMap) using
670 CRYSOL [88].

671 *Differential scanning fluorimetry*

672 Differential scanning fluorimetry experiments were carried out using Viia7 real-time PCR system
673 (Applied Biosystems) and 1× Protein Thermal Shift dye (Applied Biosystems). The assay buffer (20 mM
674 Tris pH 8.5, 500 mM NaCl, 1 mM DTT) was mixed with dye stock solution and protein solution (H_6-
675 pUL21 or H_6-pUL21^{V382E} in an 8:1:1 ratio, giving 1 ng protein in a final volume of 20 µL, and
676 measurements were performed in triplicate. Samples were heated from 25 to 95°C at 1 degree per 20 s
677 and fluorescence was monitored at each increment. The melting temperature (T_m) is the inflection point
678 of the sigmoidal melting curve, determined by non-linear curve fitting to the Boltzmann equation using
679 Prism 7 (GraphPad Software).

680 In vitro *dephosphorylation assays*

681 Dephosphorylation assays were performed upon 0.5 µM of purified CERT^P using a fixed concentration
682 of GST-PP1γ (25 nM) in the presence of pUL21-H_6 or pUL21^{V382E} -H_6 at the indicated concentrations.
683 Reactions (50 µL) proceeded in assay buffer (150 mM NaCl, 20 mM Tris pH 8.5, 0.1% TWEEN-20, 1
684 mM $MnCl_2$) for 30 min at 30°C before being stopped by the addition of 50 µL of 2× SDS-PAGE loading
685 buffer and boiling at 95°C for 5 min. Samples were analysed by SDS-PAGE using 7% (w/v) acrylamide
686 gels supplemented with 25 µM PhosTag reagent and 50 µM $MnCl_2$ and the protein was visualized using
687 InstantBlue Coomassie stain (Expedeon). To measure the ratio of CERT^O to total CERT, Coomassie-
688 stained gels were scanned using an Odyssey CLx Imaging System (LI-COR). The signals detected in
689 the 700 nm channel for the CERT^O band alone and for all CERT bands (CERT^O + CERT^P) were
690 quantitated using Image Studio Lite software (LI-COR) with local background subtraction.

691 *Plaque size analysis*

692 Confluent monolayers of Vero or HaCaT cells in 6-well tissue culture plates were infected with 100
693 plaque forming units of the indicated virus diluted in complete DMEM to a final volume of 500 µL.
694 Following the adsorption for 1 h at 37°C in a humidified 5% CO_2 atmosphere, rocking the plate every
695 15 min, the cells were overlaid with plaque assay media (DMEM supplemented with 0.3% high viscosity
696 carboxymethyl cellulose, 0.3% low viscosity carboxymethyl cellulose, 2% (v/v) FCS, 2 mM L-glutamine,
697 100 U/mL penicillin and 100 µg/mL streptomycin) and incubated for further 48 hours. Next, cells were
698 fixed with 3.7% (v/v) formal saline for 20 min, washed three times with PBS and incubated for 1 h with
699 mouse anti-gD (LP2) [76], diluted 1:50 in blocking buffer (PBS supplemented with 1% (w/v) BSA and
700 0.1% TWEEN-20). Cells were washed thrice in PBS and incubated for 30 min with HRP-conjugated
701 rabbit anti-mouse antibody (DaKo, P0161) diluted 1:5000 in blocking buffer, followed by two subsequent
702 PBS washes and one wash with ultrapure water. Plaques were visualized using the TrueBlue
703 peroxidase substrate in accordance with the manufacturer's instructions (Seracare). Plaques were
704 scanned at 1200 dpi and plaque areas were measured using Fiji [89,90].

705 *Single-step (high MOI) virus growth assays*

706 Virus growth assays were performed in technical duplicate for each independent experiment.
707 Monolayers of HaCaT or Vero cells were infected with the indicated viruses diluted in complete DMEM
708 to an MOI of 10. The time of virus addition was designated 0 hpi. After adsorption for 1 h at 37°C in a
709 humidified 5% CO_2 atmosphere, rocking the plates every 15 min, extracellular virus particles were
710 neutralized with an acid wash (40 mM citric acid, 135 mM NaCl, 10 mM KCl, pH 3.0) for 1 min and cells
711 were then washed three times with PBS before being subsequently overlaid with complete DMEM. At
712 designated times post-infection, cells were harvested by freezing the plate at -70°C. When all plates
713 were frozen, samples were freeze/thawed one more time before scraping and transferring to 1.5 mL
714 tubes and storing at -70°C until titration. Titrations were performed on monolayers of Vero cells. Serial
715 dilutions of the samples were used to inoculate the cells for 1 h, followed by overlaying with DMEM
716 containing 0.3% high viscosity carboxymethyl cellulose, 0.3% low viscosity carboxymethyl cellulose,
717 2% (v/v) FBS, 2 mM L-glutamine, 100 U/mL penicillin and 100 µg/mL streptomycin. Three days later,
718 cells were fixed in 3.7% (v/v) formal saline for 20 min, washed with water and stained with 0.1% toluidine
719 blue.

720 *Virus release assays*

721 Monolayers of HaCaT or Vero cells were infected as described above for single-step virus growth
722 assays, infections being performed in technical duplicate or triplicate for each independent experiment.
723 At 12 hpi, the media (500 µL) were harvested to 1.5 mL Eppendorf tubes, spun down for 5 min at 1000
724 g to remove any detached cells, 300 µL of the supernatant was carefully transferred to fresh tubes and
725 stored at -70°C until titration. The cells were overlaid with 500 µL of fresh DMEM and the plates were

726 immediately frozen at -70°C. Titrations were performed on monolayers of Vero cells as described
727 above.

728 *Immunocytochemistry*

729 Cells grown on #1.5 coverslips were infected at an MOI of 1 as described above. At 14 hpi, cells were
730 washed with PBS and incubated with freezing cold (-20°C) methanol for 5 min at -20°C. Coverslips
731 were washed with PBS, followed by incubation with blocking buffer (1% (w/v) BSA in PBS) for 30 min
732 at RT. Primary antibodies (above) were diluted in blocking buffer and incubated with coverslips for 1 h.
733 Coverslips were washed ten times with PBS before incubation for 45 min with the secondary antibodies
734 (above) diluted in blocking buffer. Coverslips were washed ten times in PBS and ten times in ultrapure
735 water before mounting on slides using Mowiol 4–88 (Merck) containing 200 nM 4′,6-diamidino-2-
736 phenylindole (DAPI). Images were acquired using an inverted Olympus IX81 widefield microscope with
737 a 60× Plan Apochromat N oil objective (numerical aperture 1.42) (Olympus) and Retiga EXi Fast1394
738 interline CCD camera (QImaging).

739 **Acknowledgements**

740 The synchrotron SAXS data was collected at beamline P12 operated by EMBL Hamburg at the PETRA
741 III storage ring (DESY, Hamburg, Germany). We thank Chris Boutell (MRC-University of Glasgow
742 Centre for Virus Research), John Willis (University of Pennsylvania) and David Ron (Cambridge
743 Institute for Medical Research) for kindly providing antibodies or plasmids. This work was funded by a
744 Royal Society University Research Fellowship (UF100371), a Royal Society Enhancement Award
745 (RGF\EA\180151) and a Wellcome Trust Senior Research Fellowship (219447/Z/19/Z) to JED, a
746 Biotechnology and Biological Sciences Research Council (BBSRC) Research Grant (BB/M021424/1)
747 and a Medical Research Council Research Grant (MR/T016493/1) to CMC, and by a Sir Henry Dale
748 Fellowship, jointly funded by the Wellcome Trust and the Royal Society (098406/Z/12/B) to SCG. DIS
749 and CMJ acknowledge the support of iNEXT-Discovery (project number 871037) funded by the Horizon
750 2020 programme of the European Commission. For the purpose of open access, the authors have
751 applied a Creative Commons Attribution (CC BY) licence to any Author Accepted Manuscript version
752 arising from this submission.

753 **Data availability**

754 The SAXS data measured for each concentration, with an accompanying report, are available in the
755 Small Angle Scattering Biological Data Bank (SASBDB) [91], entries SASDNB7, SASDNC7 and
756 SASDND7.

757 **Conflict of Interest**

758 The authors declare they have no conflict of interest.

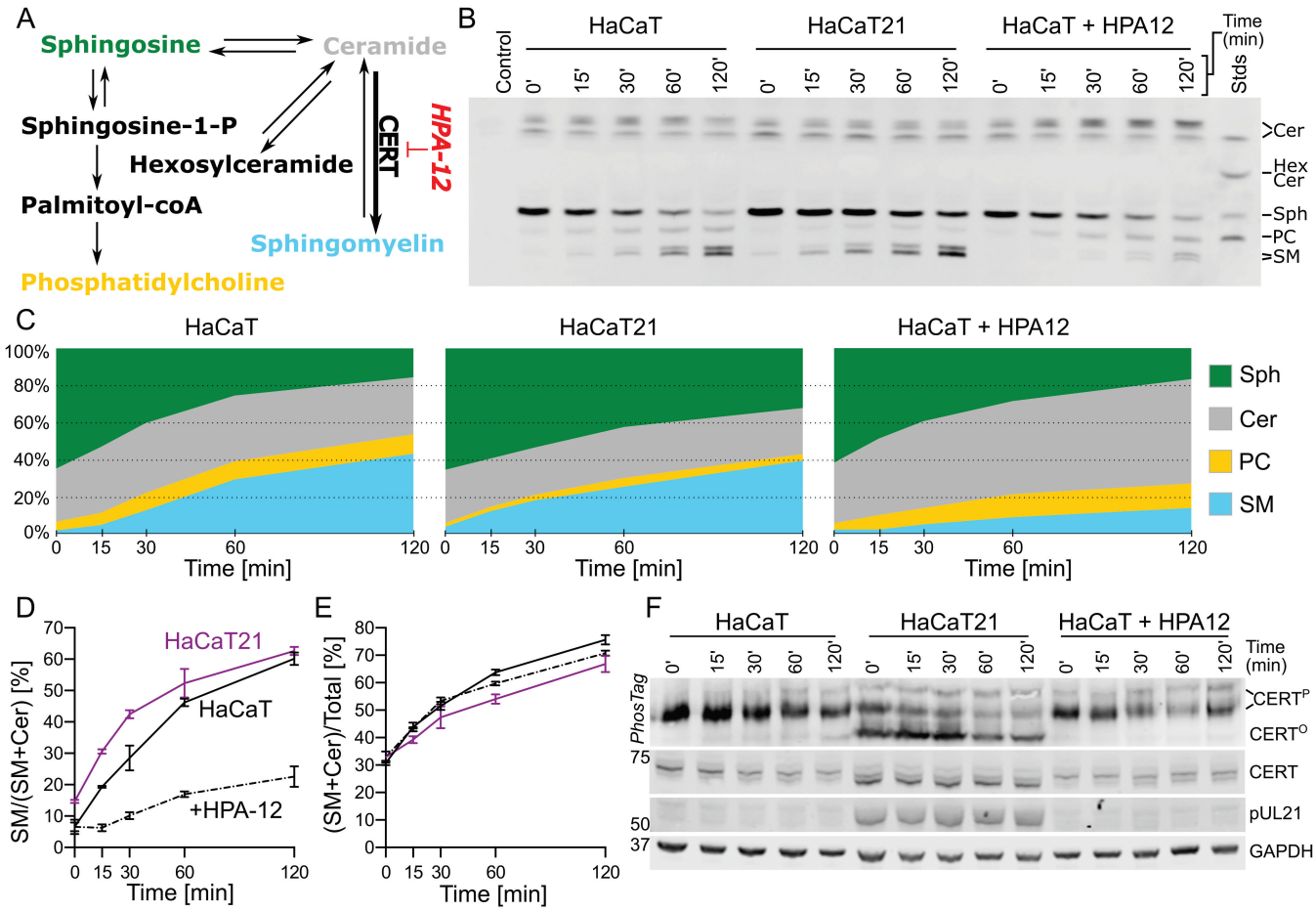

Figure 1. HSV-1 pUL21 alters the rate of ceramide to sphingomyelin conversion in cultured cells. (**A**) Simplified schematic diagram of sphingolipid biosynthetic pathways that lead from sphingosine (Sph) to sphingomyelin (SM) and glycosphingolipids (hexosylceramide; HexCer), or to phosphatidylcholine (PC) via a "salvage" pathway. Ceramide (Cer) to SM conversion is accelerated by the transport protein CERT, which is selectively inhibited by HPA-12. (**B**) Rate of Sph conversion to Cer, SM or PC was measured in HaCaT cells, untreated or treated with 1 μM HPA-12, and in HaCaT cells stably expressing pUL21 (HaCaT21). Cells were incubated with 5 μM 'clickable' alkyne-Sph (pulse) for 5 min and harvested for lipid extraction either immediately (0 min) or at the indicated times (chase). Extracted lipids were bioconjugated to 3-azido-7-hydroxycoumarin, separated by HPTLC and detected using UV light. Separated lipids were identified using clickable standards (Stds) and previous literature [42]. (**C**) Quantitation of the lipid intensities from (**B**) as determined by densitometry and represented as percentage fraction of total signal. (**D**) Rate of SM synthesis expressed as its fraction in the cumulative signal for SM and Cer. The data represents two independent experiments (mean ± SEM). (**E**) The ratio of alkyne-Sph incorporated into either Cer or SM as a proportion of total alkyne-lipid signal, representing the influx of Sph into the SM biosynthetic pathway. (**F**) The re-solubilised proteins precipitated during lipid extraction were analysed by SDS-PAGE and immunoblotting using the antibodies listed. Where indicated, the gel was supplemented with PhosTag reagent to retard the migration of phosphorylated proteins, thus enhancing the separation of CERT that is hypo- ($CERT^{O}$) or hyper-phosphorylated ($CERT^{P}$). GAPDH serves as a loading control.

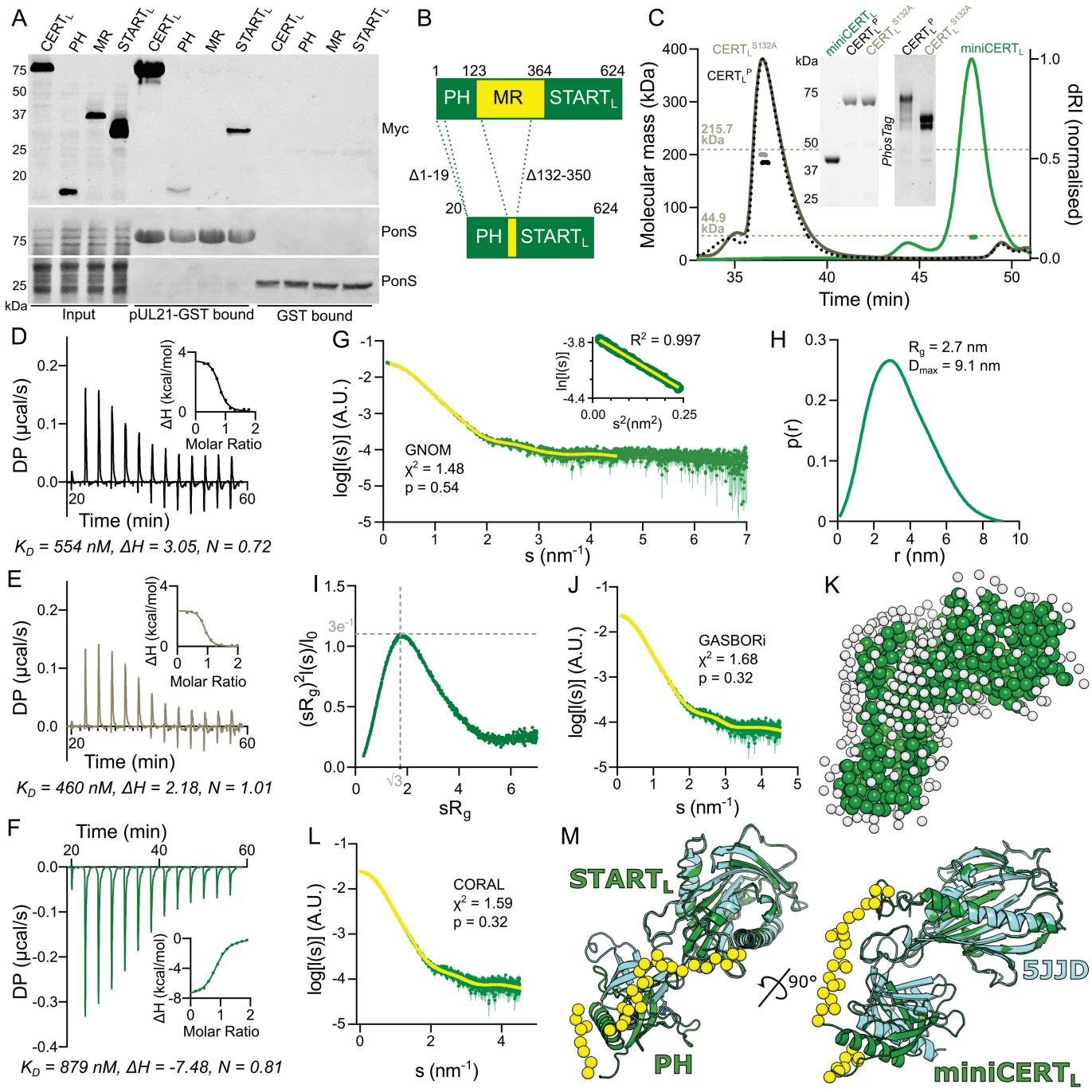

Figure 2. pUL21 binds to the PH and START$_L$ domains of CERT$_L$, and to a monomeric form of CERT$_L$ comprising just the PH and START$_L$ domains (miniCERT$_L$). (**A**) Minimal binding elements of CERT$_L$ were determined via pull down experiment using immobilised purified pUL21-GST or GST alone to capture myc-tagged full-length CERT$_L$ or truncations thereof expressed via *in vitro* transcription/translation. Captured proteins were subjected to SDS-PAGE and immunoblotting using an anti-myc antibody. Ponceau S (PonS) staining of the immunoblot membrane before blocking shows equal and efficient capture of the bait proteins across the tested conditions. (**B**) Schematic representation of miniCERT$_L$. Dotted lines indicate the regions of full-length CERT$_L$ that were omitted. (**C**) SEC-MALS elution profiles (normalized differential refractive index, dRI) of StrepII-CERT$_L$ (black dotted), StrepII-CERT$_L^{S132A}$ (grey solid) and H$_6$-miniCERT$_L$ (green solid). Weight-averaged molecular

788 masses (coloured solid lines) are shown across the elution peaks. The expected molecular masses for
789 trimeric StrepII-CERT$_L$ and StrepII-CERT$_L^{S132A}$, and for monomeric H$_6$-miniCERT$_L$, are shown as dotted
790 horizontal lines. Inset shows Coomassie-stained SDS-PAGE of the samples used for SEC-MALS (left),
791 plus SDS-PAGE supplemented with PhosTag reagent (right) of the StrepII-CERT$_L$ proteins. (**D–F**)
792 Representative ITC titration curve of pUL21-H$_6$ binding to (**D**) StrepII-CERT$_L$, (**E**) StrepII-CERT$_L^{S132A}$,
793 and (**F**) H$_6$-miniCERT$_L$. DP, differential power. Insets show normalized binding curves with integrated
794 changes in enthalpy (ΔH) as a function of molar ratio. The affinity (K_D), ΔH and stoichiometry (N) for the
795 presented titrations are displayed below. (**G**) SAXS profile measured for H$_6$-miniCERT$_L$. The reciprocal-
796 space fit of the $p(r)$ profile to the SAXS data is shown as a yellow line. χ2, fit quality; p, Correlation Map
797 (CorMap) probability of systematic deviations between the model fit and the scattering data [82]. Inset
798 shows the Guinier plot (sR_g < 1.3), which is linear as expected for an aggregate- and repulsion-free
799 system. (**H**) The real-space distance distribution function, $p(r)$, calculated from the SAXS profile. (**I**)
800 Dimensionless Kratky plot of the SAXS data. Grey dotted lines indicate the expected maximum of the
801 plot for a compact protein ($sR_g = \sqrt{3}$, $(sR_g)^2 I(s)/I(0) = 3e^{-1}$) [92]. (**J**) Fit of an *ab initio* dummy-residue
802 model calculated using GASBOR to the SAXS profile, and (**K**) representative GASBOR dummy-residue
803 model. White spheres indicate modelled water beads of the hydration shell. (**L**) Fit to the SAXS profile
804 of the pseudo-atomic model of H$_6$-miniCERT$_L$ obtained using CORAL. (**M**) CORAL pseudo-atomic
805 model of H$_6$-miniCERT$_L$ (green ribbons) superimposed onto the crystal structure of the complex
806 between the CERT PH and START domains (PDB ID 5JJD; cyan ribbons) [46] by aligning the
807 START/START$_L$ domains. Superposition is shown in orthogonal orientations where the linker regions
808 or termini that were modelled by CORAL are depicted as yellow spheres.

809

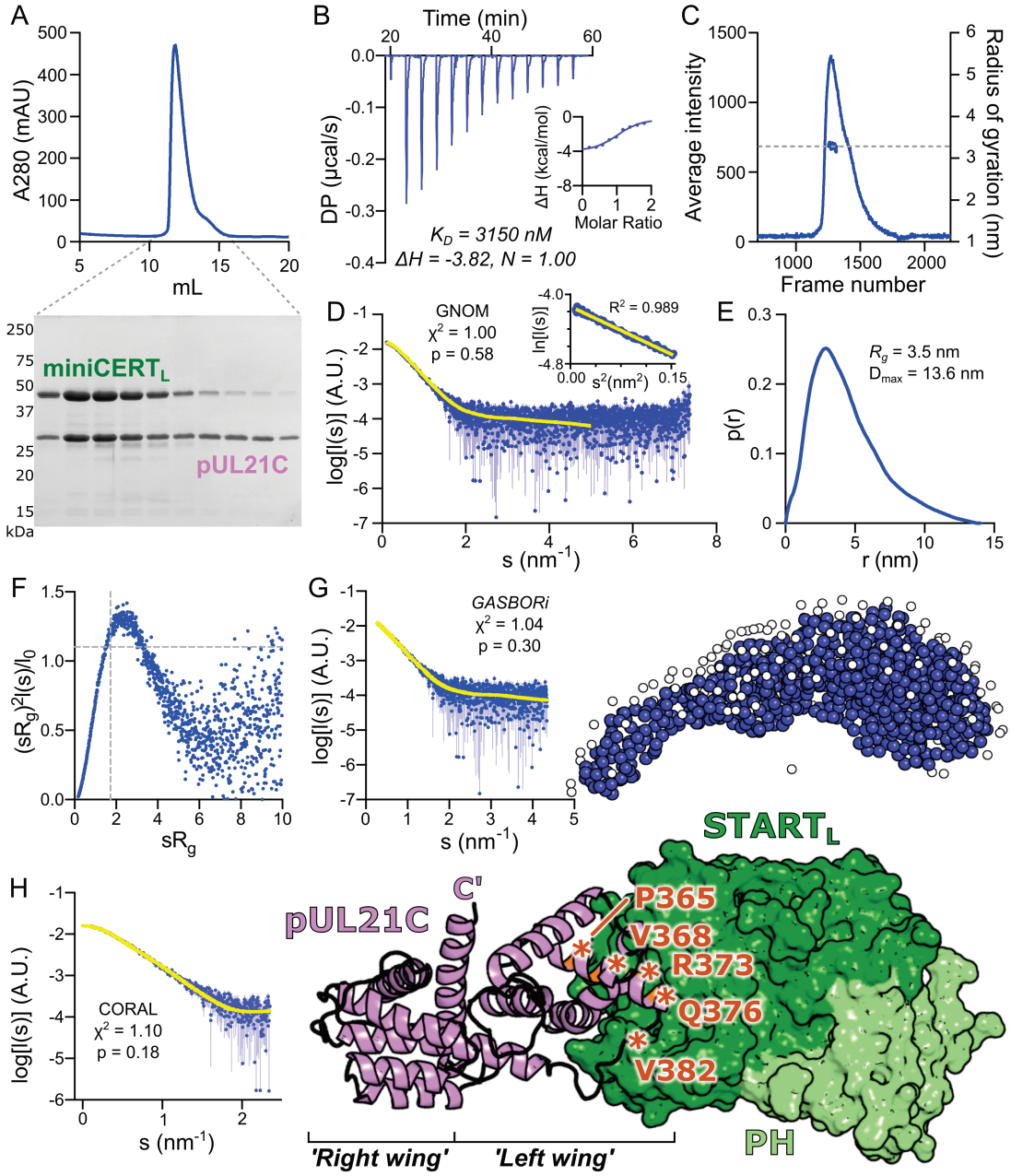

Figure 3. Solution structure of the H$_6$-pUL21C:H$_6$-miniCERT$_L$ heterodimer. (**A**) SEC elution profile (A_{280}) of the H$_6$-pUL21C:H$_6$-miniCERT$_L$ complex, pre-formed in the presence of 1.32-fold molar excess of H$_6$-pUL21C. Dotted lines indicate fractions that were collected and subjected to SDS-PAGE analysis with Coomassie staining, revealing co-elution of the two proteins. (**B**) Representative ITC titration curve of H$_6$-pUL21C binding to H$_6$-miniCERT$_L$. DP, differential power. Inset shows normalized binding curve with integrated changes in enthalpy (ΔH) as a function of molar ratio. The ranges of the vertical axes are identical to Fig 2F. The affinity (K_D), ΔH and stoichiometry (N) for the presented titration are displayed below. (**C**) SEC elution profile (partial integrated scattered X-ray intensity vs. data frame number) obtained during SEC-SAXS analysis of H$_6$-pUL21C:H$_6$-miniCERT$_L$ complex. Dashed line indicates the calculated radius of gyration (R_g) across the frames averaged for structural analyses. (**D**) Averaged SAXS profile of the H$_6$-pUL21C:H$_6$-miniCERT$_L$ complex. The reciprocal-space fit of the $p(r)$ profile to the SAXS data is shown as a yellow line. χ^2, fit quality; p, Correlation Map (CorMap) probability

822 of systematic deviations between the model fit and the scattering data [82]. Inset displays the Guinier
823 plot (sR_g < 1.3), which is linear as expected for an aggregate- and repulsion-free system. (**E**) Real-
824 space distance distribution function, $p(r)$, calculated from the SAXS profile. (**F**) Dimensionless Kratky
825 plot of the SAXS data. Grey dotted lines indicate the expected maximum of the plot for a compact
826 protein ($sR_g = \sqrt{3}$, $(sR_g)^2 I(s)/I(0) = 3e^{-1}$). (**G**) *Ab initio* modelling of H_6-miniCERT$_L$:H_6-pUL21C using
827 GASBOR. Fit of the calculated scattering (yellow) to the SAXS profile is shown, as is a representative
828 dummy-residue model (blue spheres) with modelled water beads of the hydration shell (white spheres).
829 (**H**) Pseudo-atomic model of the H_6-miniCERT$_L$:H_6-pUL21C complex generated using CORAL. The fit
830 of the computed scattering (yellow) to the SAXS profile is shown. pUL21C is shown as a violet ribbon
831 with C terminus labelled and miniCERT$_L$ as a green molecular surface (PH, light green; START$_L$, dark
832 green). The left and right 'wings' of the dragonfly-like pUL21C fold [50] are labelled. For clarity, regions
833 absent from the crystal structures that were modelled by CORAL are not displayed. Orange asterisks
834 indicate pUL21C residues at the interface with miniCERT$_L$ that were selected for further investigation.
835 Additional pseudo-atomic models that also fit the scattering data are shown in Fig S2.

836

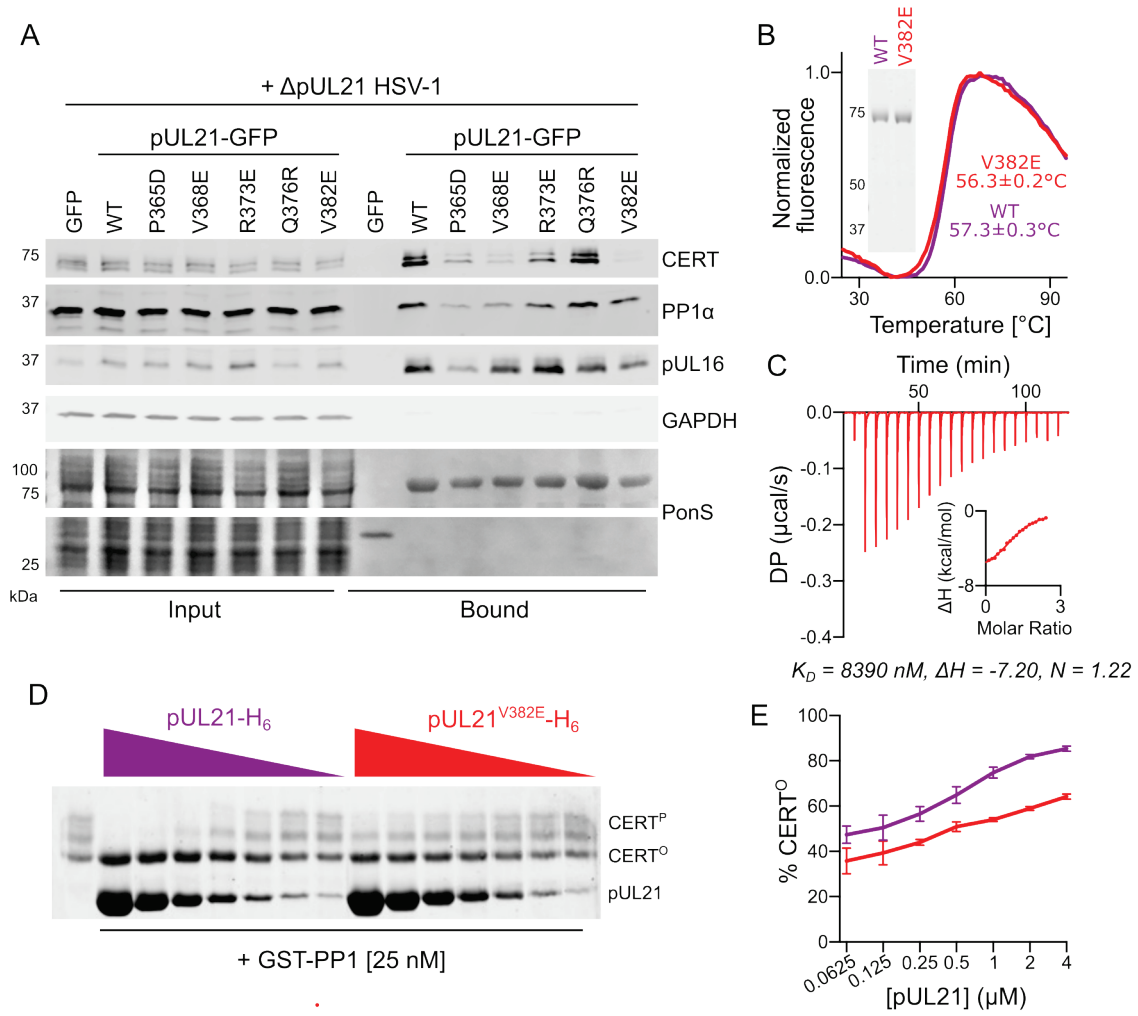

Figure 4. Identification and validation of a pUL21 point mutant with disrupted binding to CERT. (**A**) Immunoblot following immunoprecipitation from HEK293T cells transfected with plasmids encoding GFP-tagged pUL21, either wild-type (WT) or with amino acid substitutions at the putative $CERT_L$ binding interface (Figure 3H), or encoding GFP alone. At 24 hours post-transfection cells were infected with ΔpUL21 HSV-1 (MOI = 5) and at 16 hours post-infection cells were lysed, tagged proteins were captured using GFP affinity resin, and the bound proteins were subjected to SDS-PAGE and immunoblotting using the antibodies listed. Ponceau S (PonS) staining of the nitrocellulose membrane before blocking is shown to confirm efficient capture of GFP-tagged proteins. (**B**) Differential scanning fluorimetry of WT (purple) and V382E (red) pUL21-H_6. Representative curves are shown and melting temperature (T_m) is mean ± SEM of three technical replicates. Inset shows Coomassie-stained SDS-PAGE of the purified proteins. (**C**) Representative ITC titration curve of pUL21^{V382E}-H_6 binding to H_6-miniCERT$_L$. DP, differential power. Inset shows normalized binding curve with integrated changes in enthalpy (ΔH) as a function of molar ratio. The ranges of the vertical axes are identical to Fig 2F. The affinity (K_D), ΔH and stoichiometry (N) for the presented titration are displayed below. (**D**) *In vitro* dephosphorylation assay using all-purified proteins. 0.5 µM CERT^P was incubated with varying concentrations of pUL21-H_6 WT or V382E (two-fold dilution from 4 µM to 62.5 nM) in the presence of 25 nM GST-PP1 for 30 min at 30°C. Proteins were resolved using SDS-PAGE supplemented with PhosTag reagent to enhance

854 separation of CERT that is hyper- ($CERT^P$) or hypo-phosphorylated ($CERT^O$), and protein bands were
855 visualised using Coomassie. Images are representative of two independent experiments. (**E**)
856 Quantitation of concentration-dependent pUL21-mediated stimulation of CERT dephosphorylation as
857 determined by densitometry. Ratio of $CERT^O$ to total CERT ($CERT^O$+$CERT^P$) for two independent
858 experiments is shown (mean ± SEM).

859

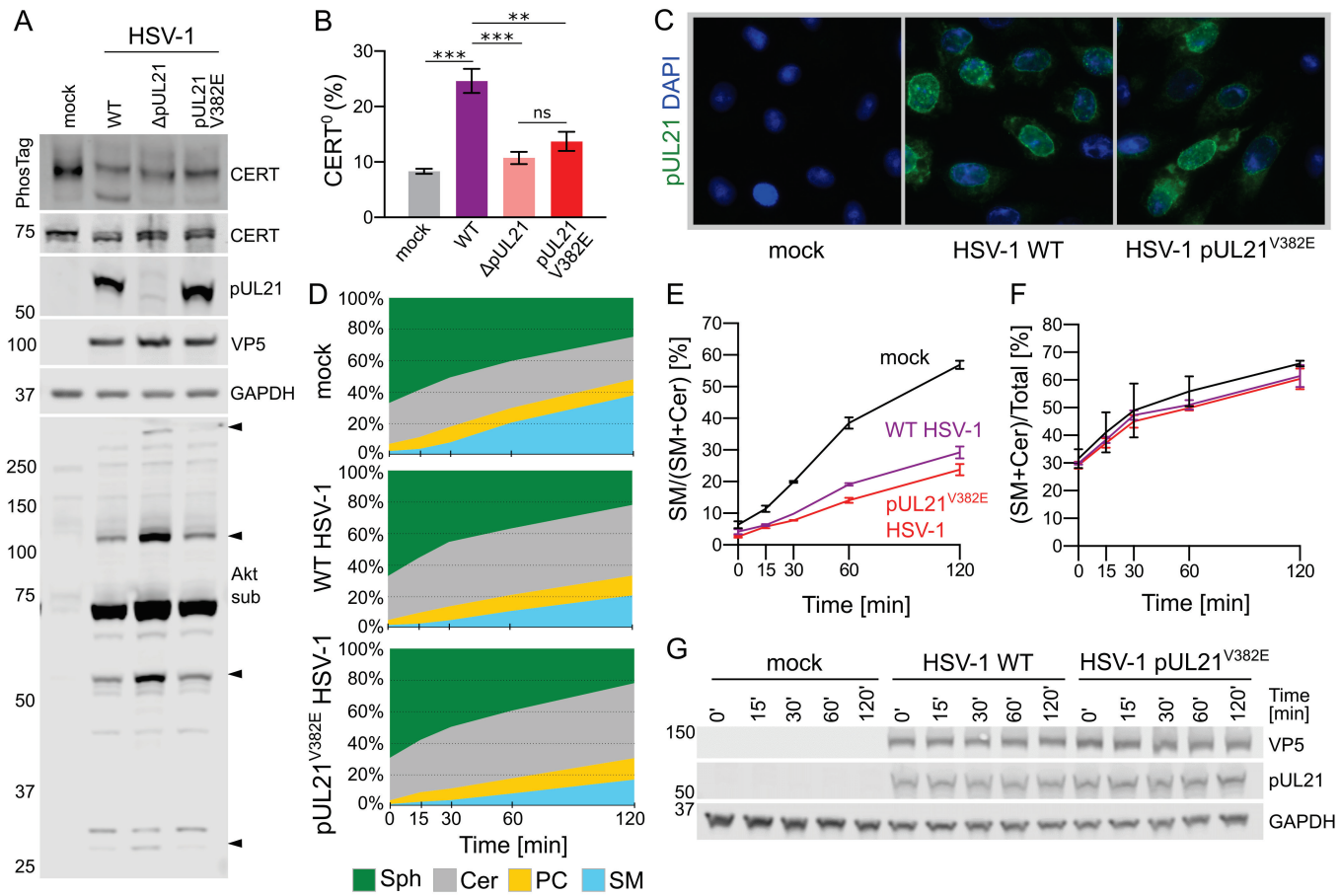

Figure 5. Mutating the CERT-binding interface of pUL21 inhibits CERT dephosphorylation and reduces the rate of sphingomyelin synthesis in infected cells. (**A**) HaCaT cells were infected at MOI = 5 with wild-type (WT) HSV-1, HSV-1 lacking pUL21 expression (ΔpUL21), or a pUL21 point mutant virus (pUL21^{V382E}). Lysates were harvested at 16 hpi in the presence of phosphatase inhibitors and subjected to SDS-PAGE plus immunoblotting using the antibodies listed. Where indicated, the gel was supplemented with PhosTag reagent to enhance separation of CERT phosphoforms. The antibody recognising phosphorylated Akt substrates (Akt sub) illustrates activity of the HSV-1 kinase pUS3, several substrates of which are dephosphorylated in a pUL21-dependent manner (arrowheads) [18]. VP5, infection control. (**B**) Quantitation of the CERT dephosphorylation level (ratio of CERT^{O} to total CERT) in cells infected with WT or mutant HSV-1, as determined by densitometry. Results are presented as mean ± SEM from three independent experiments. One-way ANOVA with Dunnett's multiple comparisons test was used for the statistical analysis (ns, non-significant; **, $p < 0.01$; ***, $p < 0.001$). (**C**) Vero cells were infected at MOI = 1, fixed 14 hpi and stained with DAPI (blue) plus an antibody recognising pUL21 (green). (**D**) Pulse-chase experiment to measure the rate of Sph conversion to Cer, SM and PC. HaCaT cells were infected with WT or pUL21^{V382E} HSV-1 at MOI = 5, or mock infected. Cells were incubated with 5 μM alkyne-Sph (pulse) at 14 hpi for 5 min and harvested for lipid extraction either immediately (0 min) or at the indicated times (chase). Extracted lipids were bioconjugated to 3-azido-7-hydroxycoumarin using click chemistry, separated by HPTLC, visualised using UV light and relative lipid abundances were quantitated by densitometry. (**E**) Rate of SM synthesis

879 expressed as its fraction in the cumulative signal for SM and Cer. (**F**) The proportion of click-Sph
880 incorporated into either Cer or SM, representing the temporal influx of Sph into the SM biosynthesis
881 pathway. For (**E**) and (**F**) the data represents two independent experiments (mean ± SEM). (**G**) The re-
882 solubilised proteins precipitated during lipid extraction were analysed by SDS-PAGE and
883 immunoblotting using the antibodies listed.

884

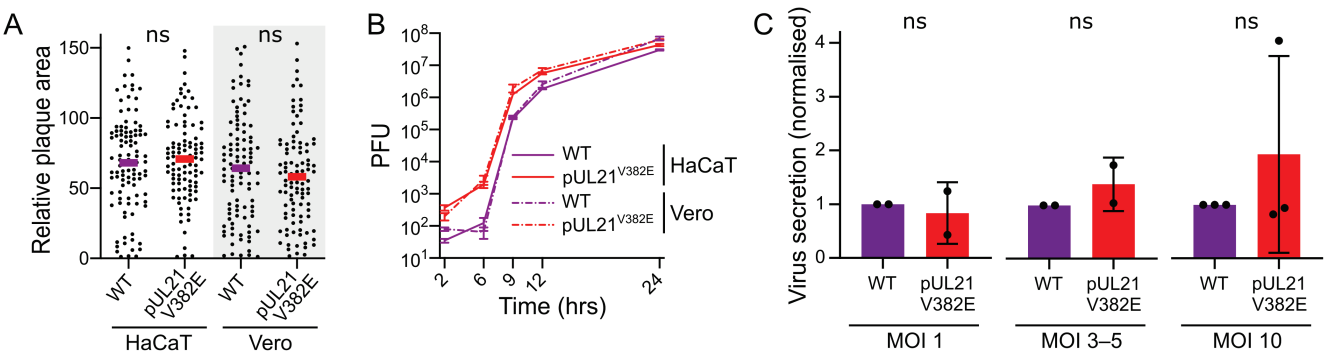

Figure 6. pUL21-mediated dephosphorylation of CERT accelerates virus replication but does not enhance virus secretion or cell-to-cell spread. (**A**) Monolayers of HaCaT or Vero cells were infected with 100 plaque forming units of WT or pUL21^{V382E} HSV-1. Following infection, cells were overlaid with medium containing 0.6% caboxymethyl cellulose and incubated for 48 hours, then fixed and immunostained with chromogenic detection. Relative plaque areas (pixels) were measured using Fiji [89,90]. Bars represent mean plaque sizes, which were compared using unpaired t-test (n=100; ns, non-significant). (**B**) Single-step (high MOI) growth curves of WT and pUL21^{V382E} HSV-1. Monolayers of HaCaT (continuous line) or Vero (dotted line) cells were infected (MOI = 5) with the viruses shown. Samples were harvested at the indicated times and titres determined by plaque assay using Vero cells. Data are presented as mean values ± SEM of technical duplicates from one representative experiment. (**C**) Virus release into the culture supernatant from HaCaT cells infected with WT or pUL21^{V382E} HSV-1 at various MOIs. Samples were harvested at 12 hpi and virus infectivity in the cells versus the culture medium was measured by titration on Vero cells. The fold change in secretion of infectivity into the culture medium for pUL21^{V382E} versus WT HSV-1 is shown as mean values ± SEM of two (MOI = 1 or 3–5) or three (MOI = 10) independent experiments. For MOI 3–5, the data represent one independent experiment performed at MOI = 3 and one at MOI = 5. For each MOI, the extent of virus secretion was compared using an unpaired t-test (ns, non-significant).

903 **Table 1. Thermodynamic properties of the pUL21:CERT$_L$ interaction**. As quantitated by isothermal
904 titration calorimetry (ITC). Experiments were performed *n* (replicates) times and mean ± SEM values
905 are shown.

Syringe	Cell	K_D [nM]	ΔH [kcal/mol]	ΔG [kcal/mol]	-TΔS [kcal/mol]	N (stoichiometry)	*n* (replicates)
CERT$_L^P$	pUL21	772.67 ± 158.18	3.89 ± 0.74	-8.37 ± 0.11	-12.27 ± 0.62	0.74 ± 0.01	3
CERT$_L^{S132A}$	pUL21	642.0 ± 182.0	2.385 ± 0.21	-8.475 ± 0.18	-10.85 ± 0.05	0.97 ± 0.04	2
miniCERT$_L$	pUL21	1042.0 ± 240.46	-8.65 ± 0.28	-8.21 ± 0.11	0.44 ± 0.35	0.89 ± 0.03	6
miniCERT$_L$	pUL21C	4325.0 ± 1175.0	-3.84 ± 0.02	-7.35 ± 0.17	-3.51 ± 0.18	0.97 ± 0.03	2
miniCERT$_L$	pUL21^{V382E}	8086.67 ± 538.53	-7.20 ± 0.03	-6.95 ± 0.04	0.26 ± 0.01	1.16 ± 0.08	3

906

907 **References**

908 1. Looker KJ, Magaret AS, May MT, Turner KME, Vickerman P, Gottlieb SL, et al. Global and
909 Regional Estimates of Prevalent and Incident Herpes Simplex Virus Type 1 Infections in 2012.
910 PloS One. 2015;10: e0140765. doi:10.1371/journal.pone.0140765

911 2. Kulej K, Avgousti DC, Sidoli S, Herrmann C, Fera AND, Kim ET, et al. Time-resolved Global and
912 Chromatin Proteomics during Herpes Simplex Virus Type 1 (HSV-1) Infection. Mol Cell
913 Proteomics MCP. 2017;16: S92. doi:10.1074/mcp.M116.065987

914 3. Nahas KL, Connor V, Scherer KM, Kaminski CF, Harkiolaki M, Crump CM, et al. Near-native state
915 imaging by cryo-soft-X-ray tomography reveals remodelling of multiple cellular organelles during
916 HSV-1 infection. BioRχiv. 2022. doi:10.1101/2021.10.11.463900

917 4. Soh TK, Davies CTR, Muenzner J, Hunter LM, Barrow HG, Connor V, et al. Temporal Proteomic
918 Analysis of Herpes Simplex Virus 1 Infection Reveals Cell-Surface Remodeling via pUL56-
919 Mediated GOPC Degradation. Cell Rep. 2020;33: 108235. doi:10.1016/j.celrep.2020.108235

920 5. Scherer KM, Manton JD, Soh TK, Mascheroni L, Connor V, Crump CM, et al. A fluorescent
921 reporter system enables spatiotemporal analysis of host cell modification during herpes simplex
922 virus-1 replication. J Biol Chem. 2021;296: 100236. doi:10.1074/jbc.RA120.016571

923 6. Bigalke JM, Heldwein EE. Nuclear Exodus: Herpesviruses Lead the Way. Annu Rev Virol. 2016;3:
924 387–409. doi:10.1146/annurev-virology-110615-042215

925 7. Owen DJ, Crump CM, Graham SC. Tegument Assembly and Secondary Envelopment of
926 Alphaherpesviruses. Viruses. 2015;7: 5084–5114. doi:10.3390/v7092861

927 8. Cocchi F, Menotti L, Dubreuil P, Lopez M, Campadelli-Fiume G. Cell-to-Cell Spread of Wild-Type
928 Herpes Simplex Virus Type 1, but Not of Syncytial Strains, Is Mediated by the Immunoglobulin-
929 Like Receptors That Mediate Virion Entry, Nectin1 (PRR1/HveC/HIgR) and Nectin2
930 (PRR2/HveB). J Virol. 2000;74: 3909–3917. doi:10.1128/JVI.74.8.3909-3917.2000

931 9. Le Sage V, Jung M, Alter JD, Wills EG, Johnston SM, Kawaguchi Y, et al. The herpes simplex
932 virus 2 UL21 protein is essential for virus propagation. J Virol. 2013;87: 5904–5915.
933 doi:10.1128/JVI.03489-12

934 10. Harper AL, Meckes DG, Marsh JA, Ward MD, Yeh P-C, Baird NL, et al. Interaction domains of the
935 UL16 and UL21 tegument proteins of herpes simplex virus. J Virol. 2010;84: 2963–2971.
936 doi:10.1128/JVI.02015-09

937 11. Klupp BG, Böttcher S, Granzow H, Kopp M, Mettenleiter TC. Complex formation between the
938 UL16 and UL21 tegument proteins of pseudorabies virus. J Virol. 2005;79: 1510–1522.
939 doi:10.1128/JVI.79.3.1510-1522.2005

940 12. Han J, Chadha P, Starkey JL, Wills JW. Function of glycoprotein E of herpes simplex virus
941 requires coordinated assembly of three tegument proteins on its cytoplasmic tail. Proc Natl Acad
942 Sci. 2012;109: 19798–19803. doi:10.1073/pnas.1212900109

943 13. Takakuwa H, Goshima F, Koshizuka T, Murata T, Daikoku T, Nishiyama Y. Herpes simplex virus
944 encodes a virion-associated protein which promotes long cellular processes in over-expressing
945 cells. Genes Cells. 2001;6: 955–966. doi:10.1046/j.1365-2443.2001.00475.x

946 14. Yan K, Liu J, Guan X, Yin Y-X, Peng H, Chen H-C, et al. The Carboxyl Terminus of Tegument
947 Protein pUL21 Contributes to Pseudorabies Virus Neuroinvasion. J Virol. 2019;93: 02052–18.
948 doi:10.1128/JVI.02052-18

949 15. Finnen RL, Banfield BW. CRISPR/Cas9 Mutagenesis of UL21 in Multiple Strains of Herpes
950 Simplex Virus Reveals Differential Requirements for pUL21 in Viral Replication. Viruses. 2018;10.
951 doi:10.3390/v10050258

952 16. Sarfo A, Starkey J, Mellinger E, Zhang D, Chadha P, Carmichael J, et al. The UL21 Tegument
953 Protein of Herpes Simplex Virus 1 Is Differentially Required for the Syncytial Phenotype. J Virol.
954 2017;91: 01161–17. doi:10.1128/JVI.01161-17

955 17. Klupp BG, Lomniczi B, Visser N, Fuchs W, Mettenleiter TC. Mutations affecting the UL21 gene
956 contribute to avirulence of pseudorabies virus vaccine strain Bartha. Virology. 1995;212: 466–
957 473. doi:10.1006/viro.1995.1504

958 18. Benedyk TH, Muenzner J, Connor V, Han Y, Brown K, Wijesinghe KJ, et al. pUL21 is a viral
959 phosphatase adaptor that promotes herpes simplex virus replication and spread. PLOS Pathog.
960 2021;17: e1009824. doi:10.1371/journal.ppat.1009824

961 19. Peti W, Nairn AC, Page R. Structural basis for protein phosphatase 1 regulation and specificity.
962 FEBS J. 2013;280: 596–611. doi:10.1111/j.1742-4658.2012.08509.x

963 20. Muradov JH, Finnen RL, Gulak MA, Hay TJM, Banfield BW. pUL21 regulation of pUs3 kinase
964 activity influences the nature of nuclear envelope deformation by the HSV-2 nuclear egress
965 complex. PLoS Pathog. 2021;17: e1009679. doi:10.1371/journal.ppat.1009679

966 21. Fukasawa M, Nishijima M, Hanada K. Genetic evidence for ATP-dependent endoplasmic
967 reticulum-to-Golgi apparatus trafficking of ceramide for sphingomyelin synthesis in Chinese
968 hamster ovary cells. J Cell Biol. 1999;144: 673–685. doi:10.1083/jcb.144.4.673

969 22. Funakoshi T, Yasuda S, Fukasawa M, Nishijima M, Hanada K. Reconstitution of ATP- and cytosol-
970 dependent transport of de novo synthesized ceramide to the site of sphingomyelin synthesis in
971 semi-intact cells. J Biol Chem. 2000;275: 29938–29945. doi:10.1074/jbc.M004470200

972 23. Hanada K, Kumagai K, Yasuda S, Miura Y, Kawano M, Fukasawa M, et al. Molecular machinery
973 for non-vesicular trafficking of ceramide. Nature. 2003;426: 803–809. doi:10.1038/nature02188

974 24. Prashek J, Truong T, Yao X. Crystal Structure of the Pleckstrin Homology Domain from the
975 Ceramide Transfer Protein: Implications for Conformational Change upon Ligand Binding. PLoS
976 ONE. 2013;8: e79590. doi:10.1371/journal.pone.0079590

977 25. Kudo N, Kumagai K, Tomishige N, Yamaji T, Wakatsuki S, Nishijima M, et al. Structural basis for
978 specific lipid recognition by CERT responsible for nonvesicular trafficking of ceramide. Proc Natl
979 Acad Sci. 2008;105: 488–493. doi:10.1073/pnas.0709191105

980 26. Charruyer A, Bell SM, Kawano M, Douangpanya S, Yen T-Y, Macher BA, et al. Decreased
981 Ceramide Transport Protein (CERT) Function Alters Sphingomyelin Production following UVB
982 Irradiation. J Biol Chem. 2008;283: 16682–16692. doi:10.1074/jbc.M800799200

983 27. Kawano M, Kumagai K, Nishijima M, Hanada K. Efficient trafficking of ceramide from the
984 endoplasmic reticulum to the Golgi apparatus requires a VAMP-associated protein-interacting
985 FFAT motif of CERT. J Biol Chem. 2006;281: 30279–30288. doi:10.1074/jbc.M605032200

986 28. Kumagai K, Kawano M, Shinkai-Ouchi F, Nishijima M, Hanada K. Interorganelle trafficking of
987 ceramide is regulated by phosphorylation-dependent cooperativity between the PH and START
988 domains of CERT. J Biol Chem. 2007;282: 17758–17766. doi:10.1074/jbc.M702291200

989 29. Hannun YA, Obeid LM. Sphingolipids and their metabolism in physiology and disease. Nat Rev
990 Mol Cell Biol. 2018;19: 175–191. doi:10.1038/nrm.2017.107

991 30. Sezgin E, Levental I, Mayor S, Eggeling C. The mystery of membrane organization: composition,
992 regulation and roles of lipid rafts. Nat Rev Mol Cell Biol. 2017;18: 361–374.
993 doi:10.1038/nrm.2017.16

994 31. Olsen ASB, Faergeman NJ. Sphingolipids: membrane microdomains in brain development,
995 function and neurological diseases. Open Biol. 2017;7: 170069. doi:10.1098/rsob.170069

996 32. Elwell CA, Engel JN. Lipid acquisition by intracellular Chlamydiae. Cell Microbiol. 2012;14: 1010–
997 1018. doi:10.1111/j.1462-5822.2012.01794.x

998 33. Gewaid H, Aoyagi H, Arita M, Watashi K, Suzuki R, Sakai S, et al. Sphingomyelin Is Essential for
999 the Structure and Function of the Double-Membrane Vesicles in Hepatitis C Virus RNA
1000 Replication Factories. J Virol. 2020;94: e01080-20. doi:10.1128/JVI.01080-20

1001 34. Ray EK, Blough HA. The effect of herpesvirus infection and 2-deoxy-d-glucose on
1002 glycosphingolipids in BHK-21 cells. Virology. 1978;88: 118–127. doi:10.1016/0042-
1003 6822(78)90115-0

1004 35. Steinhart WL, Busch JS, Oettgen JP, Howland JL. Sphingolipid metabolism during infection of
1005 human fibroblasts by herpes simplex virus type 1. Intervirology. 1984;21: 70–76.
1006 doi:10.1159/000149504

1007 36. Pastenkos G, Miller JL, Pritchard SM, Nicola AV. Role of Sphingomyelin in Alphaherpesvirus
1008 Entry. J Virol. 2019;93: e01547-18. doi:10.1128/JVI.01547-18

1009 37. Lang J, Bohn P, Bhat H, Jastrow H, Walkenfort B, Cansiz F, et al. Acid ceramidase of
1010 macrophages traps herpes simplex virus in multivesicular bodies and protects from severe
1011 disease. Nat Commun. 2020;11: 1338. doi:10.1038/s41467-020-15072-8

1012 38. Roussel E, Lippe R. Cellular Protein Kinase D Modulators Play a Role during Multiple Steps of
1013 Herpes Simplex Virus 1 Egress. J Virol. 2018;92: e01486-18. doi:10.1128/JVI.01486-18

1014 39. Shevchenko A, Simons K. Lipidomics: coming to grips with lipid diversity. Nat Rev Mol Cell Biol.
1015 2010;11: 593–598. doi:10.1038/nrm2934

1016 40. Sunshine H, Iruela-Arispe ML. Membrane Lipids and Cell Signaling. Curr Opin Lipidol. 2017;28:
1017 408–413. doi:10.1097/MOL.0000000000000443

1018 41. Gaebler A, Milan R, Straub L, Hoelper D, Kuerschner L, Thiele C. Alkyne lipids as substrates for
1019 click chemistry-based in vitro enzymatic assays. J Lipid Res. 2013;54: 2282–2290.
1020 doi:10.1194/jlr.D038653

1021 42. Gerl MJ, Bittl V, Kirchner S, Sachsenheimer T, Brunner HL, Lüchtenborg C, et al. Sphingosine-1-
1022 Phosphate Lyase Deficient Cells as a Tool to Study Protein Lipid Interactions. PLOS ONE.
1023 2016;11: e0153009. doi:10.1371/journal.pone.0153009

1024 43. Morash SC, Cook HW, Spence MW. Lysophosphatidylcholine as an intermediate in
1025 phosphatidylcholine metabolism and glycerophosphocholine synthesis in cultured cells: an
1026 evaluation of the roles of 1-acyl- and 2-acyl-lysophosphatidylcholine. Biochim Biophys Acta.
1027 1989;1004: 221–229. doi:10.1016/0005-2760(89)90271-3

1028 44. Yasuda S, Kitagawa H, Ueno M, Ishitani H, Fukasawa M, Nishijima M, et al. A Novel Inhibitor of
1029 Ceramide Trafficking from the Endoplasmic Reticulum to the Site of Sphingomyelin Synthesis. J
1030 Biol Chem. 2001;276: 43994–44002. doi:10.1074/jbc.M104884200

1031 45. Prischi F, Filippakopoulos P. Editorial: Structural Studies of Protein Complexes in Signaling
1032 Pathways. Front Mol Biosci. 2021;8: 200. doi:10.3389/fmolb.2021.641932

1033 46. Prashek J, Bouyain S, Fu M, Li Y, Berkes D, Yao X. Interaction between the PH and START
1034 domains of ceramide transfer protein competes with phosphatidylinositol 4-phosphate binding by
1035 the PH domain. J Biol Chem. 2017;292: 14217–14228. doi:10.1074/jbc.M117.780007

1036 47. Sugiki T, Takeuchi K, Yamaji T, Takano T, Tokunaga Y, Kumagai K, et al. Structural Basis for the
1037 Golgi Association by the Pleckstrin Homology Domain of the Ceramide Trafficking Protein
1038 (CERT). J Biol Chem. 2012;287: 33706–33718. doi:10.1074/jbc.M112.367730

1039 48. Raya A, Revert-Ros F, Martinez-Martinez P, Navarro S, Roselló E, Vieites B, et al. Goodpasture
1040 Antigen-binding Protein, the Kinase That Phosphorylates the Goodpasture Antigen, Is an
1041 Alternatively Spliced Variant Implicated in Autoimmune Pathogenesis. J Biol Chem. 2000;275:
1042 40392–40399. doi:10.1074/jbc.M002769200

1043 49. Svergun DI, Petoukhov MV, Koch MHJ. Determination of Domain Structure of Proteins from X-
1044 Ray Solution Scattering. Biophys J. 2001;80: 2946–2953. doi:10.1016/S0006-3495(01)76260-1

1045 50. Metrick CM, Heldwein EE. Novel Structure and Unexpected RNA-Binding Ability of the C-Terminal
1046 Domain of Herpes Simplex Virus 1 Tegument Protein UL21. J Virol. 2016;90: 5759–5769.
1047 doi:10.1128/JVI.00475-16

1048 51. Metrick CM, Chadha P, Heldwein EE. The unusual fold of herpes simplex virus 1 UL21, a
1049 multifunctional tegument protein. J Virol. 2015;89: 2979–2984. doi:10.1128/JVI.03516-14

1050 52. Tischer BK, Smith GA, Osterrieder N. En passant mutagenesis: a two step markerless red
1051 recombination system. Methods Mol Biol Clifton NJ. 2010;634: 421–430. doi:10.1007/978-1-
1052 60761-652-8_30

1053 53. Chuluunbaatar U, Roller R, Feldman ME, Brown S, Shokat KM, Mohr I. Constitutive mTORC1
1054 activation by a herpesvirus Akt surrogate stimulates mRNA translation and viral replication. Genes
1055 Dev. 2010;24: 2627–2639. doi:10.1101/gad.1978310

1056 54. Roussel É, Lippé R. Cellular Protein Kinase D Modulators Play a Role during Multiple Steps of
1057 Herpes Simplex Virus 1 Egress. J Virol. 2018;92: e01486-18. doi:10.1128/JVI.01486-18

1058 55. Bell C, Desjardins M, Thibault P, Radtke K. Proteomics analysis of herpes simplex virus type 1-
1059 infected cells reveals dynamic changes of viral protein expression, ubiquitylation, and
1060 phosphorylation. J Proteome Res. 2013;12: 1820–1829. doi:10.1021/pr301157j

1061 56. Jean Beltran PM, Cook KC, Hashimoto Y, Galitzine C, Murray LA, Vitek O, et al. Infection-Induced
1062 Peroxisome Biogenesis Is a Metabolic Strategy for Herpesvirus Replication. Cell Host Microbe.
1063 2018;24: 526-541.e7. doi:10.1016/j.chom.2018.09.002

1064 57. Langeland N, Haarr L, Holmsen H. Polyphosphoinositide metabolism in baby-hamster kidney cells
1065 infected with herpes simplex virus type 1. Biochem J. 1986;237: 707–712. doi:10.1042/bj2370707

1066 58. Sutter E, de Oliveira AP, Tobler K, Schraner EM, Sonda S, Kaech A, et al. Herpes simplex virus
1067 1 induces de novo phospholipid synthesis. Virology. 2012;429: 124–135.
1068 doi:10.1016/j.virol.2012.04.004

1069 59. Han X. Lipidomics for studying metabolism. Nat Rev Endocrinol. 2016;12: 668–679.
1070 doi:10.1038/nrendo.2016.98

1071 60. Xu T, Hu C, Xuan Q, Xu G. Recent advances in analytical strategies for mass spectrometry-based
1072 lipidomics. Anal Chim Acta. 2020;1137: 156–169. doi:10.1016/j.aca.2020.09.060

1073 61. Campadelli G, Brandimarti R, Lazzaro CD, Ward PL, Roizman B, Torrisi MR. Fragmentation and
1074 dispersal of Golgi proteins and redistribution of glycoproteins and glycolipids processed through

1075 the Golgi apparatus after infection with herpes simplex virus 1. Proc Natl Acad Sci. 1993;90:
1076 2798–2802. doi:10.1073/pnas.90.7.2798

1077 62. Kumagai K, Hanada K. Structure, functions and regulation of CERT, a lipid-transfer protein for the
1078 delivery of ceramide at the ER-Golgi membrane contact sites. FEBS Lett. 2019;593: 2366–2377.
1079 doi:10.1002/1873-3468.13511

1080 63. Rémillard-Labrosse G, Mihai C, Duron J, Guay G, Lippé R. Protein kinase D-dependent trafficking
1081 of the large Herpes simplex virus type 1 capsids from the TGN to plasma membrane. Traffic Cph
1082 Den. 2009;10: 1074–1083. doi:10.1111/j.1600-0854.2009.00939.x

1083 64. Alonso A, Goñi FM. The Physical Properties of Ceramides in Membranes. Annu Rev Biophys.
1084 2018;47: 633–654. doi:10.1146/annurev-biophys-070317-033309

1085 65. Bigalke JM, Heldwein EE. Structural basis of membrane budding by the nuclear egress complex
1086 of herpesviruses. EMBO J. 2015;34: 2921–2936. doi:10.15252/embj.201592359

1087 66. Thorsen MK, Lai A, Lee MW, Hoogerheide DP, Wong GCL, Freed JH, et al. Highly Basic Clusters
1088 in the Herpes Simplex Virus 1 Nuclear Egress Complex Drive Membrane Budding by Inducing
1089 Lipid Ordering. mBio. 12: e01548-21. doi:10.1128/mBio.01548-21

1090 67. Ogretmen B. Sphingolipid metabolism in cancer signalling and therapy. Nat Rev Cancer. 2018;18:
1091 33–50. doi:10.1038/nrc.2017.96

1092 68. Galvan V, Roizman B. Herpes simplex virus 1 induces and blocks apoptosis at multiple steps
1093 during infection and protects cells from exogenous inducers in a cell-type-dependent manner.
1094 Proc Natl Acad Sci U S A. 1998;95: 3931–3936. doi:10.1073/pnas.95.7.3931

1095 69. Li Z, Michael IP, Zhou D, Nagy A, Rini JM. Simple piggyBac transposon-based mammalian cell
1096 expression system for inducible protein production. Proc Natl Acad Sci U S A. 2013;110: 5004–
1097 5009. doi:10.1073/pnas.1218620110

1098 70. Zufferey R, Donello JE, Trono D, Hope TJ. Woodchuck hepatitis virus posttranscriptional
1099 regulatory element enhances expression of transgenes delivered by retroviral vectors. J Virol.
1100 1999;73: 2886–2892. doi:10.1128/JVI.73.4.2886-2892.1999

1101 71. Neidel S, Maluquer de Motes C, Mansur DS, Strnadova P, Smith GL, Graham SC. Vaccinia virus
1102 protein A49 is an unexpected member of the B-cell Lymphoma (Bcl)-2 protein family. J Biol Chem.
1103 2015;290: 5991–6002. doi:10.1074/jbc.M114.624650

1104 72. Chen R, Rato C, Yan Y, Crespillo-Casado A, Clarke HJ, Harding HP, et al. G-actin provides
1105 substrate-specificity to eukaryotic initiation factor 2α holophosphatases. eLife. 2015;4.
1106 doi:10.7554/eLife.04871

1107 73. Boukamp P, Petrussevska RT, Breitkreutz D, Hornung J, Markham A, Fusenig NE. Normal
1108 keratinization in a spontaneously immortalized aneuploid human keratinocyte cell line. J Cell Biol.
1109 1988;106: 761–771. doi:10.1083/jcb.106.3.761

1110 74. Carmichael JC, Wills JW. Differential Requirements for gE, gI, and UL16 among Herpes Simplex
1111 Virus 1 Syncytial Variants Suggest Unique Modes of Dysregulating the Mechanism of Cell-to-Cell
1112 Spread. J Virol. 2019;93. doi:10.1128/JVI.00494-19

1113 75. McClelland DA, Aitken JD, Bhella D, McNab D, Mitchell J, Kelly SM, et al. pH reduction as a trigger
1114 for dissociation of herpes simplex virus type 1 scaffolds. J Virol. 2002;76: 7407–7417.
1115 doi:10.1128/jvi.76.15.7407-7417.2002

76. Minson AC, Hodgman TC, Digard P, Hancock DC, Bell SE, Buckmaster EA. An analysis of the biological properties of monoclonal antibodies against glycoprotein D of herpes simplex virus and identification of amino acid substitutions that confer resistance to neutralization. J Gen Virol. 1986;67: 1001–1013. doi:10.1099/0022-1317-67-6-1001

77. Gierasch WW, Zimmerman DL, Ward SL, VanHeyningen TK, Romine JD, Leib DA. Construction and characterization of bacterial artificial chromosomes containing HSV-1 strains 17 and KOS. J Virol Methods. 2006;135: 197–206. doi:10.1016/j.jviromet.2006.03.014

78. Blanchet CE, Spilotros A, Schwemmer F, Graewert MA, Kikhney A, Jeffries CM, et al. Versatile sample environments and automation for biological solution X-ray scattering experiments at the P12 beamline (PETRA III, DESY). J Appl Crystallogr. 2015;48: 431–443. doi:10.1107/S160057671500254X

79. Graewert MA, Franke D, Jeffries CM, Blanchet CE, Ruskule D, Kuhle K, et al. Automated pipeline for purification, biophysical and x-ray analysis of biomacromolecular solutions. Sci Rep. 2015;5: 10734. doi:10.1038/srep10734

80. Wilkins MR, Gasteiger E, Bairoch A, Sanchez JC, Williams KL, Appel RD, et al. Protein identification and analysis tools in the ExPASy server. Methods Mol Biol Clifton NJ. 1999;112: 531–552. doi:10.1385/1-59259-584-7:531

81. Panjkovich A, Svergun DI. CHROMIXS: automatic and interactive analysis of chromatography-coupled small-angle X-ray scattering data. Bioinformatics. 2018;34: 1944–1946. doi:10.1093/bioinformatics/btx846

82. Franke D, Jeffries CM, Svergun DI. Correlation Map, a goodness-of-fit test for one-dimensional X-ray scattering spectra. Nat Methods. 2015;12: 419–422. doi:10.1038/nmeth.3358

83. Manalastas-Cantos K, Konarev PV, Hajizadeh NR, Kikhney AG, Petoukhov MV, Molodenskiy DS, et al. ATSAS 3.0: expanded functionality and new tools for small-angle scattering data analysis. J Appl Crystallogr. 2021;54: 343–355. doi:10.1107/S1600576720013412

84. Svergun DI. Determination of the regularization parameter in indirect-transform methods using perceptual criteria. J Appl Crystallogr. 1992;25: 495–503. doi:10.1107/S0021889892001663

85. Hajizadeh NR, Franke D, Jeffries CM, Svergun DI. Consensus Bayesian assessment of protein molecular mass from solution X-ray scattering data. Sci Rep. 2018;8: 7204. doi:10.1038/s41598-018-25355-2

86. Petoukhov MV, Franke D, Shkumatov AV, Tria G, Kikhney AG, Gajda M, et al. New developments in the ATSAS program package for small-angle scattering data analysis. J Appl Crystallogr. 2012;45: 342–350. doi:10.1107/S0021889812007662

87. Yang J, Yan R, Roy A, Xu D, Poisson J, Zhang Y. The I-TASSER Suite: protein structure and function prediction. Nat Methods. 2015;12: 7–8. doi:10.1038/nmeth.3213

88. Svergun D, Barberato C, Koch MHJ. *CRYSOL* – a Program to Evaluate X-ray Solution Scattering of Biological Macromolecules from Atomic Coordinates. J Appl Crystallogr. 1995;28: 768–773. doi:10.1107/S0021889895007047

89. Rueden CT, Schindelin J, Hiner MC, DeZonia BE, Walter AE, Arena ET, et al. ImageJ2: ImageJ for the next generation of scientific image data. BMC Bioinformatics. 2017;18: 529. doi:10.1186/s12859-017-1934-z

90. Schindelin J, Arganda-Carreras I, Frise E, Kaynig V, Longair M, Pietzsch T, et al. Fiji: an open-source platform for biological-image analysis. Nat Methods. 2012;9: 676–682. doi:10.1038/nmeth.2019

91. Valentini E, Kikhney AG, Previtali G, Jeffries CM, Svergun DI. SASBDB, a repository for biological small-angle scattering data. Nucleic Acids Res. 2015;43: D357-363. doi:10.1093/nar/gku1047

92. Receveur-Brechot V, Durand D. How random are intrinsically disordered proteins? A small angle scattering perspective. Curr Protein Pept Sci. 2012;13: 55–75. doi:10.2174/138920312799277901